

CONCENTRATIONS OF DARK HALOS FROM THEIR ASSEMBLY HISTORIES

RISA H. WECHSLER¹, JAMES S. BULLOCK², JOEL R. PRIMACK¹, ANDREY V. KRAVTSOV^{2,3},
AVISHAI DEKEL⁴,

Submitted 2001 August 9; last revision 2001 October 26

ABSTRACT

We study the relation between the density profiles of dark matter halos and their mass assembly histories, using a statistical sample of halos in a high-resolution N-body simulation of the Λ CDM cosmology. For each halo at $z = 0$, we identify its merger-history tree, and determine concentration parameters c_{vir} for all progenitors, thus providing a structural merger tree for each halo. We fit the mass accretion histories by a universal function with one parameter, the formation epoch a_c , defined when the log mass accretion rate $d \log M / d \log a$ falls below a critical value S . We find that late forming galaxies tend to be less concentrated, such that c_{vir} “observed” at any epoch a_o is strongly correlated with a_c via $c_{\text{vir}} = c_1 a_o / a_c$. Scatter about this relation is mostly due to measurement errors in c_{vir} and a_c , implying that the actual spread in c_{vir} for halos of a given mass can be mostly attributed to scatter in a_c . We demonstrate that this relation can also be used to predict the mass and redshift dependence of c_{vir} , and the scatter about the median $c_{\text{vir}}(M, z)$, using accretion histories derived from the Extended Press-Schechter (EPS) formalism, after adjusting for a constant offset between the formation times as predicted by EPS and as measured in the simulations; this new ingredient can thus be easily incorporated into semi-analytic models of galaxy formation. The correlation found between halo concentration and mass accretion rate suggests a physical interpretation: for high mass infall rates the central density is related to the background density; when the mass infall rate slows, the central density stays approximately constant and the halo concentration just grows as R_{vir} . Because of the direct connection between halo concentration and velocity rotation curves, and because of probable connections between halo mass assembly history and star formation history, the tight correlation between these properties provides an essential new ingredient for galaxy formation modeling.

Subject headings: cosmology:theory — galaxies:halos — galaxies:formation — galaxies:evolution — galaxies:structure — dark matter

1. INTRODUCTION

The theory of cold dark matter (CDM) (e.g., Peebles 1982; Blumenthal et al. 1984; Davis et al. 1985) provides a remarkably successful framework for understanding galaxy assembly and structure formation in the universe. Within this picture, dark matter collapses first into small halos, and these halos merge to form progressively larger halos over time. As this process continues, baryons that initially trace the dark matter cool and condense to form galaxies in halo centers. New supplies of gas and galaxy mergers are closely linked to the mass accretion histories of the halos they inhabit. A detailed understanding of how this mass accretion occurs, and how individual halo properties depend on their merger histories, is of fundamental importance for predicting galaxy properties within the CDM theory, and, similarly, for using observed galaxy properties (e.g., rotation curves) to test the paradigm.

The basic theory for the buildup of structure in the universe, and for the evolution of the properties of gravitationally-bound structures, is fairly well developed; it has been extensively simulated at increasingly high resolution, and analytic formulations have been developed to describe this behavior. The Press-Schechter formalism

(Press & Schechter 1974; Bond et al. 1991) has provided a useful framework for understanding the mass function of dark halos, and, with subsequent improvements, has been shown to work well in comparison to N-body simulations (Gross et al. 1998; Sheth & Tormen 1999; Sheth, Mo, & Tormen 2001; Jenkins et al. 2001; Sheth & Tormen 2001). The theory has been extended using an excursion-set formalism to an Extended Press-Schechter theory (EPS), which describes the statistics of the buildup of individual halos through time (Bond et al. 1991; Lacey & Cole 1993). This EPS theory has been implemented to construct random realizations of merger trees, each specifying a full assembly history for a halo (e.g., Lacey & Cole 1993; Kauffmann et al. 1993; Somerville & Kolatt 1999, hereafter SK99). Detailed comparisons of EPS with simulations have highlighted the general success of the theory and quantified the level of accuracy of its predictions (e.g., Somerville et al. 2000, hereafter SLKD; Gardner 2001; Cohn, Bagla, & White 2001).

Similar advances have been made in understanding halo density structure (Efstathiou et al. 1988; Frenk et al. 1988; Dubinski & Carlberg 1991). Navarro, Frenk, & White (1995,1996,1997; hereafter NFW), have proposed that halo

¹ Physics Department, University of California, Santa Cruz, CA 95064; wechsler@umich.edu, joel@ucolick.org

² Department of Astronomy, The Ohio State University, 140 W. 18th Ave, Columbus, OH 43210; james@astronomy.ohio-state.edu, andrey@oddjob.uchicago.edu

³ Hubble Fellow

⁴ Racah Institute of Physics, The Hebrew University, Jerusalem 91904 Israel; dekel@astro.huji.ac.il

profiles can be universally fit by a two-parameter functional form:

$$\rho_{\text{NFW}}(r) = \frac{\rho_s}{(r/R_s)(1+r/R_s)^2}, \quad (1)$$

where R_s is a characteristic “inner” radius, and ρ_s a corresponding inner density. One of the inner parameters can be replaced by a “virial” parameter, either the virial radius (R_{vir}), mass (M_{vir}), or velocity (V_{vir}), defined such that the mean density inside the virial radius is Δ_{vir} times the mean universal density ρ_u at that redshift:

$$M_{\text{vir}} \equiv \frac{4\pi}{3} \Delta_{\text{vir}} \rho_u R_{\text{vir}}^3. \quad (2)$$

The critical overdensity at virialization, Δ_{vir} , is motivated by the spherical collapse model; it has a value $\simeq 180$ for the Einstein-deSitter cosmology, and $\simeq 340$ for the Λ CDM cosmology assumed here. A useful alternative parameter for describing the shape of the profile is the concentration parameter c_{vir} , defined as $c_{\text{vir}} \equiv R_{\text{vir}}/R_s$. NFW found that this functional form provides a good fit to halos over two decades in radius, for a large range of halo masses, and for several different cosmological scenarios. They tested it for the Einstein-deSitter model with a standard CDM power spectrum of initial fluctuations (SCDM), a flat cosmological model with $\Omega_m = 0.3$, $\Omega_\Lambda = 0.7$ and a corresponding CDM power spectrum (Λ CDM), and several models with power-law power spectra (confirmed by Craig 1997, and Kravtsov, Klypin, & Khokhlov 1997).

Later studies (e.g., Moore et al. 1998; Ghigna et al. 2000; Klypin et al. 2001) have indicated that the inner logarithmic slopes of at least some halo density profiles in CDM cosmologies are closer to -1.5 than to -1.0 .¹ However, Klypin et al. (2001) showed that even for halos that are better fit by -1.5 slopes, an NFW fit is perfectly adequate outside the inner $\sim 1\%$ of the virial radius (this corresponds to roughly $\sim 3\text{kpc}$ for a Milky-Way type halo). An important implication (as pointed out by Bullock et al. 2001, hereafter B01) is that even if halos are not perfectly described by the NFW form (see also Avila-Reese et al. 1999 and Jing 2000), fit parameters derived using this profile provide a useful general characterization of the density structure, relating, for example, the central density of a halo to that of the background via two fit parameters (e.g., c_{vir} and R_{vir}).

The two-parameter NFW characterization of halo profiles has provided several useful insights into the nature of halo collapse. Among the most interesting results, first noticed by NFW, was that, for a given cosmology, the central density ρ_s varies inversely with halo mass, or, equivalently, c_{vir} tends to increase with decreasing M_{vir} . A natural reason for this fact is that low-mass halos typically collapse earlier, when the universe was denser, and the central density somehow reflects this higher background density.² In a toy model to explain this correlation, NFW (1997) assumed that ρ_s is a constant multiple k of the universal density $\rho_u(z_c)$ at a collapse redshift z_c . They defined the collapse redshift as the time when half of the halo’s mass was first in progenitors more massive than f times the halo’s mass. The general trend of the relation between the

two profile parameters at $z = 0$ is reproduced well using EPS to predict z_c , and a proper choice of values for the constants k and f (favored parameters for Λ CDM were $f = 0.01$ and $k = 3.4 \times 10^3$).

Subsequent analyses revealed additional complexities and trends in halo structure. First, it has been realized that while the $M_{\text{vir}}-c_{\text{vir}}$ trend holds on average, halos of fixed mass show significant scatter in their c_{vir} values (Bullock 1999; Jing 2000; B01). In the context of the proposed correlation between concentration and collapse time, the scatter in c_{vir} is a natural reflection of the expected scatter in collapse time for halos of a given mass.

B01 also found that halo concentrations (at fixed mass) are systematically lower at higher redshifts, $c_{\text{vir}} \propto 1/(1+z)$, implying a much stronger trend than that predicted by the NFW toy model. Since by definition the concentration at redshift z roughly relates the halo central density to the universal background density at that time via $c_{\text{vir}}(z) \propto [\rho_c(z)/\bar{\rho}(z)]^{1/3}$, we have $c_{\text{vir}}(z) \propto \rho_c(z)^{1/3}/(1+z)$. The observed relation implies that a halo’s central density (or collapse time) is set only by the halo’s mass, *independent of the redshift when the halo is observed*. One reason for the shortcoming of the NFW toy model in reproducing the proper redshift dependence is that the collapse time as defined by this model also depends on the redshift of observation. In order to properly match the time evolution, B01 proposed a modified toy model in which the collapse time, denoted now by \tilde{a}_c (instead of a_c to avoid later confusion) is set by the mass only, and is defined as the epoch at which the typical collapsing mass, $M_*(\tilde{a}_c)$, equals a fixed fraction F of the halo mass at epoch a , $M_*(\tilde{a}_c) \equiv FM_{\text{vir}}$. The typical collapsing mass is defined by $\sigma[M_*(a)] = 1.686/D(a)$, where $\sigma(M)$ is the rms density fluctuation on the comoving scale encompassing a mass M , extrapolated using linear theory to the present, $a = 1$, and $D(a)$ is the linear growth rate. The implied concentration is given by $c_{\text{vir}}(a) = Ka/\tilde{a}_c$, which, with appropriate values of F and K , reproduces quite well the dependence of concentration on both mass and redshift as measured in simulations (see B01 for details).

Simplified models of the type discussed so far provide a qualitative understanding and useful parameterization of the complex processes seen in simulations (for further insights and an exploration of non-hierarchical power spectra see Eke et al. 2001). However, our understanding remains somewhat schematic and several important questions remain open. First, how do *individual* halo density profiles build up over time? How do the mass accretion histories affect the final halo concentrations, and how can physically realistic mass accretion histories be connected to the simplified definition of formation time advocated by B01? Can EPS be used to predict halo concentrations? What physical process is responsible for the scatter in c_{vir} at fixed mass? This work builds on the work of B01, using the same simulations analyzed there, together with a new “structural merger tree” described below. The goal is to see if we can directly correlate the assembly history of halos with their dark matter halo density profiles, test

¹ The opposite suggestion has also been made: that the asymptotic slope as $r \rightarrow 0$ may be somewhat shallower than -1.0 (Taylor & Navarro 2001).

² Indeed, for models with truncated power spectra, in which there is no systematic relation between collapse time and halo mass, no correlation is seen between mass and c_{vir} (Avila-Reese et al. 2001; Bode, Ostriker, & Turok 2001; Eke, Navarro, & Steinmetz 2001).

the model proposed by B01, and develop a physical model for the range of halo concentrations seen in simulations, including scatter and dependence on mass and redshift.

These questions are interesting from a theoretical perspective, but they also have direct observational implications. The shape of the halo density profile directly affects the rotation curve of the galaxy that forms within it; the one-sigma scatter in concentration observed by B01 corresponds to, for a $1 \times 10^{11} h^{-1} M_{\odot}$ halo, a scatter in V_{\max} values of $\sim 85 - 105$ km/s. Thus scatter in halo density profiles is directly related to scatter in the Tully-Fisher relation, and also has implications for the relative contributions of halo and disk to velocity rotation curves. In addition, density profiles may affect other aspects of the galaxy formation process, such as the efficiency of gas cooling or the star formation rate. If halo concentrations are related to their mass assembly histories, it may indicate that halo concentration is correlated with galaxy type. This would have implications for both the zero-point and scatter in the Tully-Fisher relation, and could also have implications for the rotation curves of low-surface brightness galaxies. Possible correlations between halo density profiles and galaxy observables (with the exception of mass) have been neglected in previous modeling efforts, but it is clear that such correlations are likely to be quite important.

We begin in §2 by summarizing the relevant details of the N-body simulation, halo finder and density profile fitting. In §3, the “structural merger tree” developed for this project is described. We continue in §4 by detailing how mass accretion histories are constructed and then describe a new method for defining a characteristic formation epoch for each halo. We then show how this formation epoch can be related to the halo concentration, and how this can explain the dependence of concentration on mass and redshift as well as explaining the origin and magnitude of the scatter in these relations. In §8, we show how Extended Press-Schechter theory can be used to predict concentrations for individual halos using our model for relating halo concentration to characteristic formation epoch. This model can reproduce the scatter, mass and redshift trends observed in N-body simulations. In §9, we discuss the scatter in $c_{\text{vir}}(M_{\text{vir}})$, and how it depends on the merging history of halos. We discuss the implications of our results and conclude in §10.

2. SIMULATED HALOS

In the work that follows, we consider only one cosmology whose evolution has been simulated with the ART code (Kravtsov, Klypin, & Khokhlov 1997), a flat Λ CDM model with $\Omega_m = 0.3$, $h = 0.7$ and $\sigma_8 = 1.0$. The simulation is the same as that used in B01. It followed the trajectories of 256^3 cold dark matter particles within a cubic, periodic box of comoving size $60h^{-1}$ Mpc from redshift $z = 40$ to the present. A 512^3 uniform grid is used, with up to six refinement levels in the regions of highest density, implying a dynamic range of 32,768. The formal resolution of the simulation is thus $f_{\text{res}} = 1.8h^{-1}$ kpc, and the mass per particle is $m_p = 1.1 \times 10^9 h^{-1} M_{\odot}$. For the purpose of constructing accurate merger trees, here we analyze the simulation data from 36 output times thinly

spaced between $z = 7$ and 0. It should be noted that the

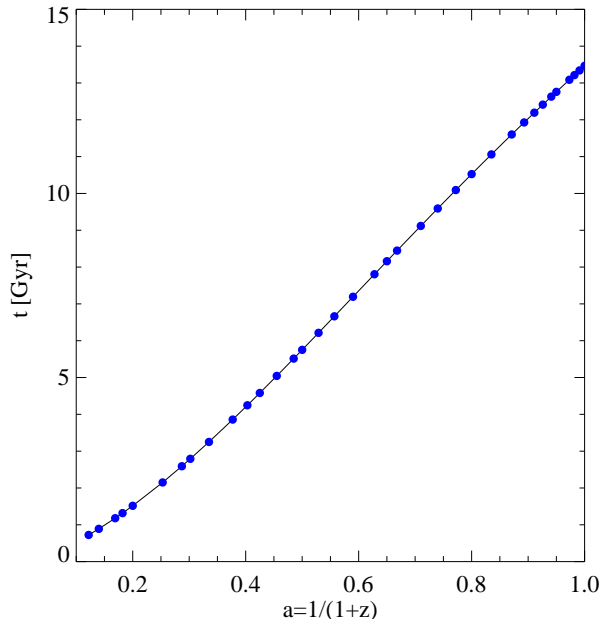


FIG. 1.— Output times of the simulation. The curve is the age of the universe t as a function of the universal expansion factor a for the Λ CDM model considered here. The symbols mark the 36 output times of the simulation.

methods described here for finding and fitting halos and constructing merger trees are completely generalizable to other simulations or cosmologies.

The halo finding algorithm used here is based on the Bound Density Maxima (Klypin & Holtzman 1997) technique described in Bullock (1999) and B01, but we have modified and optimized it for the purpose of building a structural merger tree. The essential elements are presented briefly here, and details are described in the Appendix. For each density maximum, we step out in radial shells until the mean overdensity falls below $\Delta_{\text{vir}}(z)$,³ or the radial profile shows a significant upturn. We denote this radius as R_h and the mass determined by counting particles within this radius as M_h . We attempt to identify halos containing as few as $N_p^{\text{min}} = 20$ particles; our halo catalog thus includes ~ 14000 halos above a mass threshold of $2.2 \times 10^{10} h^{-1} M_{\odot}$. By comparing our simulation with a smaller, higher resolution realization of the same cosmology, at this mass we estimate our completeness to be 70%, and we are $\sim 100\%$ complete at $6.6 \times 10^{10} h^{-1} M_{\odot}$. NFW profiles are fit to halos with more than $N_{p,\text{fit}}^{\text{min}} = 200$ particles, corresponding to halos more massive than $2.2 \times 10^{11} h^{-1} M_{\odot}$. A profile fit to a halo of only a few hundred particles carries large errors, but as long as the fit is done properly to include these errors, reliable concentrations estimates can be obtained (B01). Halos in the mass range $2 \times 10^{11} - 5 \times 10^{11} h^{-1} M_{\odot}$ have typical fit mass errors of about 10%, and c_{vir} errors of 15-20%. However, a few percent of the time the errors are significantly larger than that. We therefore make a rigorous attempt to estimate the errors and take them into account in every step of the process. Poor fits are marked

³ For flat cosmologies, Δ_{vir} can be approximated by (Bryan & Norman 1998) $\Delta_{\text{vir}} \simeq (18\pi^2 + 82x - 39x^2)/\Omega(z)$, where $x \equiv \Omega(z) - 1$, and $\Omega(z)$ is the ratio of mean matter density to critical density at redshift z ; for the Λ CDM model considered here, $\Delta_{\text{vir}} \simeq 337$.

by large errors that are incorporated in the analysis and the results we present. The outcome at any output time is a statistical halo catalog that includes all the bound virialized systems in the simulation above the mass threshold of $2.2 \times 10^{10} h^{-1} M_{\odot}$. At $z = 0$ there are 14,219 such halos. The output for each halo includes the list of its bound particles, the location and velocity of its center, and the NFW profile parameters (e.g., c_{vir} and M_{vir}) and corresponding errors (σ_c and σ_M) when applicable. (We also include information about the halo angular momentum properties; this is not used in the present work, but see also Wechsler 2001, Vitvitska et al. 2001 and Wechsler et al. in prep). The mass function of this revised halo catalog, and a detailed comparison with the halo catalog used in the work of B01, has been presented in Wechsler (2001).

3. CONSTRUCTING A MERGER TREE

As a base for the structural merger tree, we use the distinct halo catalogs described above at each of 36 output times of the simulations, from $z = 7$ to the present. The output times are well spaced in redshift; the cosmological scale factors associated with the saved output times are shown in Figure 1. Between each set of output times, we track the trajectories of all of the particles. Given a halo and an output time, we tag all of its particles and track them back to the previous output time. We then make a list of all halos at that earlier output time containing tagged particles, recording the number of tagged particles contained in each one. A similar list of halos and tagged particle numbers is obtained for the neighboring future output time. In addition, we record the number of particles that are not in any halo in the previous output time, and the number of particles that do not end up in a halo in the subsequent output time.

We have two criteria for halo 1 at one output time to be labeled a “progenitor” of halo 2 at the subsequent output time. In our language, halo 2 will then be labeled an “offspring” of halo 1. First, more than half the particles in halo 1 must end up in halo 2. In addition, since, on occasion, a halo’s particles do not end up in any halo in the subsequent output time, we also demand that more than 70% of the particles in halo 1 which end up in any halo must end up in halo 2. Thus a halo is allowed to have only one offspring, but there is no limit on the number of progenitors a halo may have. In much of the work that follows, we will focus on a “most massive progenitor” halo in the previous output time. In general, this is the progenitor halo which contributes the largest number of particles; however if the halo’s progenitor mass is not at least half of its mass, we additionally require that the progenitor’s most bound particle is included in the halo. Even if this is the case, we also check that the halo’s most bound particle in the present output time was a member of the progenitor; if it was not, the halo is only designated as the most massive progenitor if it is more massive than the minimum mass of the halo catalog and it is least a third the mass of the offspring halo. These criteria were designed to maximize the redshift extent of as many mass accretion trajectories as possible, without counting trajectories which may have been affected by the completeness of the catalog or severe errors in fitting.

We have used the criteria outlined above to construct

the merger tree of every halo at every output time. Examples of such a merger tree are shown in Figure 2, which shows the mass accumulation history of a small cluster halo of mass $M_{\text{vir}} = 2.8 \times 10^{14} h^{-1} M_{\odot}$ at $z = 0$, and a galaxy-mass halo ($M_{\text{vir}} = 2.9 \times 10^{12} h^{-1} M_{\odot}$ at $z = 0$). Each halo in the tree is represented by two circles, one with radius proportional to the halo’s virial radius and one with radius proportional to the halo’s best-fit NFW R_s parameter.

4. MASS GROWTH CURVES

For the purposes of understanding the evolution of halo concentrations, it is useful to characterize the history of mass assembly in each halo by tracking the evolution of its most massive progenitor. The mass assigned to the most massive progenitor at each output time is typically the best fit virial mass, M_{vir} . However, for cases in which the fit errors on M_{vir} were large, we used an iterative procedure, described in the appendix, to determine a corrected mass; this mass is based on either the fit mass, the measured mass within R_{vir} , or an interpolated mass between the previous and subsequent timesteps. In addition, our halo mass trajectories do not always extend as far back as the first analyzed output time of the simulation. This usually happens because the most massive progenitor at some redshift falls below our completeness limit and cannot be identified, although there are also rare cases in which our criteria for progenitor are simply not met (see Wechsler 2001). In order to have complete trajectories for a reasonable number of halos, and in order to have reliable fits for most halos, we limit our analysis to halos more massive than $10^{12} h^{-1} M_{\odot}$ at $z = 0$. In this mass range, which includes ~ 900 halos, $\sim 95\%$ of the halo trajectories extend back to $z = 2$, and $\sim 90\%$ extend back to $z = 3$.

Figure 3 shows the history of mass growth for the major progenitors of several different halos, spanning a range of masses and concentration parameters. Notice that more massive halos tend show substantial mass accumulation up to late times, but the growth curves for less massive halos tend to flatten out earlier. This tendency is illustrated in Figure 4, which shows the average mass accretion histories for halos binned by final mass. Again, the high mass halos form later than low mass halos, as expected in CDM models.

Since mass accretion is a continuous process, the loose term “formation time” is ambiguous and it requires an agreed, measurable, quantitative definition. The trends of formation time with mass and redshift may depend on this definition. One common choice is to set the formation time equal to the time when the mass in progenitor halos (or in the most massive progenitor) is equal to some fraction of the halo’s final mass M_o (e.g., NFW 1997, Lacey & Cole 1993). Definitions of this type have a common feature: the formation time is a relative measure which depends, for a given halo trajectory, on the redshift z_o at which the halo is observed. As z_o is increased, the formation redshift z_f also increases. However, it increases more slowly, since mass accretion proceeds more rapidly at high redshift in CDM models. Thus both the formation redshift z_f and the ratio of $(1 + z_f)/(1 + z_o)$ change with time in such a model. As mentioned in the introduction, this feature of the formation time definition is the reason that

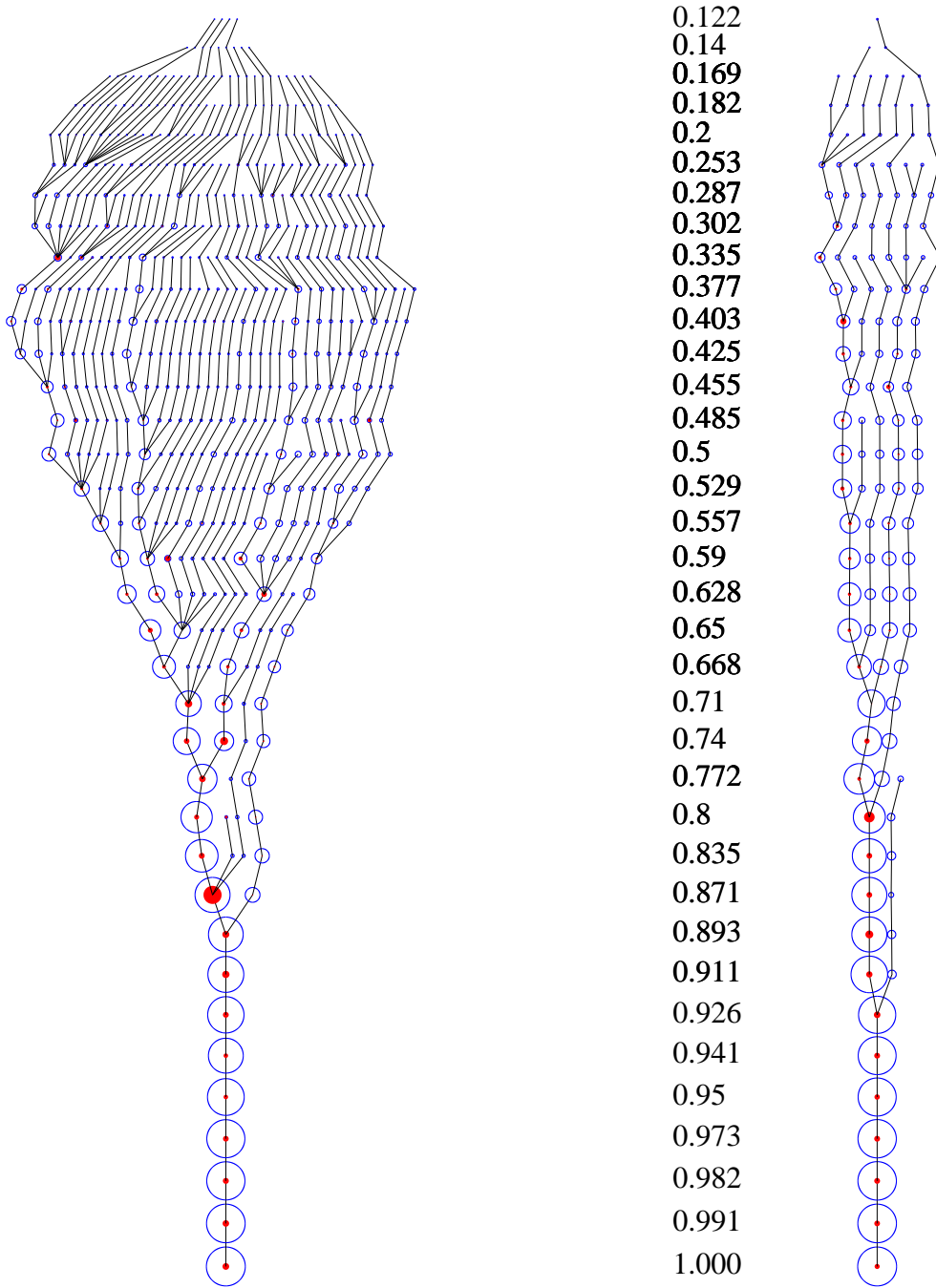


FIG. 2.— Structural merger trees for two halos. This diagram illustrates the merging history of a cluster-mass halo (left; $M_{\text{vir}} = 2.8 \times 10^{14} h^{-1} M_{\odot}$ and $c_{\text{vir}} = 5.9$) and a galaxy-mass halo (right; $M_{\text{vir}} = 2.9 \times 10^{12} h^{-1} M_{\odot}$ and $c_{\text{vir}} = 12.5$) at $a = 1$. The radii of the outer and inner (filled) circles are proportional to the virial and inner NFW radii, R_{vir} and R_s , respectively, scaled such that the two halos have equal sizes at $a = 1$. Lines connect halos with their progenitor halos. All progenitors with profile fits ($M > 2.2 \times 10^{11} h^{-1} M_{\odot}$) are shown for the cluster-mass halo; all progenitors ($M > 2.2 \times 10^{10} h^{-1} M_{\odot}$) are shown for the galaxy-mass halo. The scalefactor a at the output time is listed in the center of the plot. The width of the diagram is arbitrary.

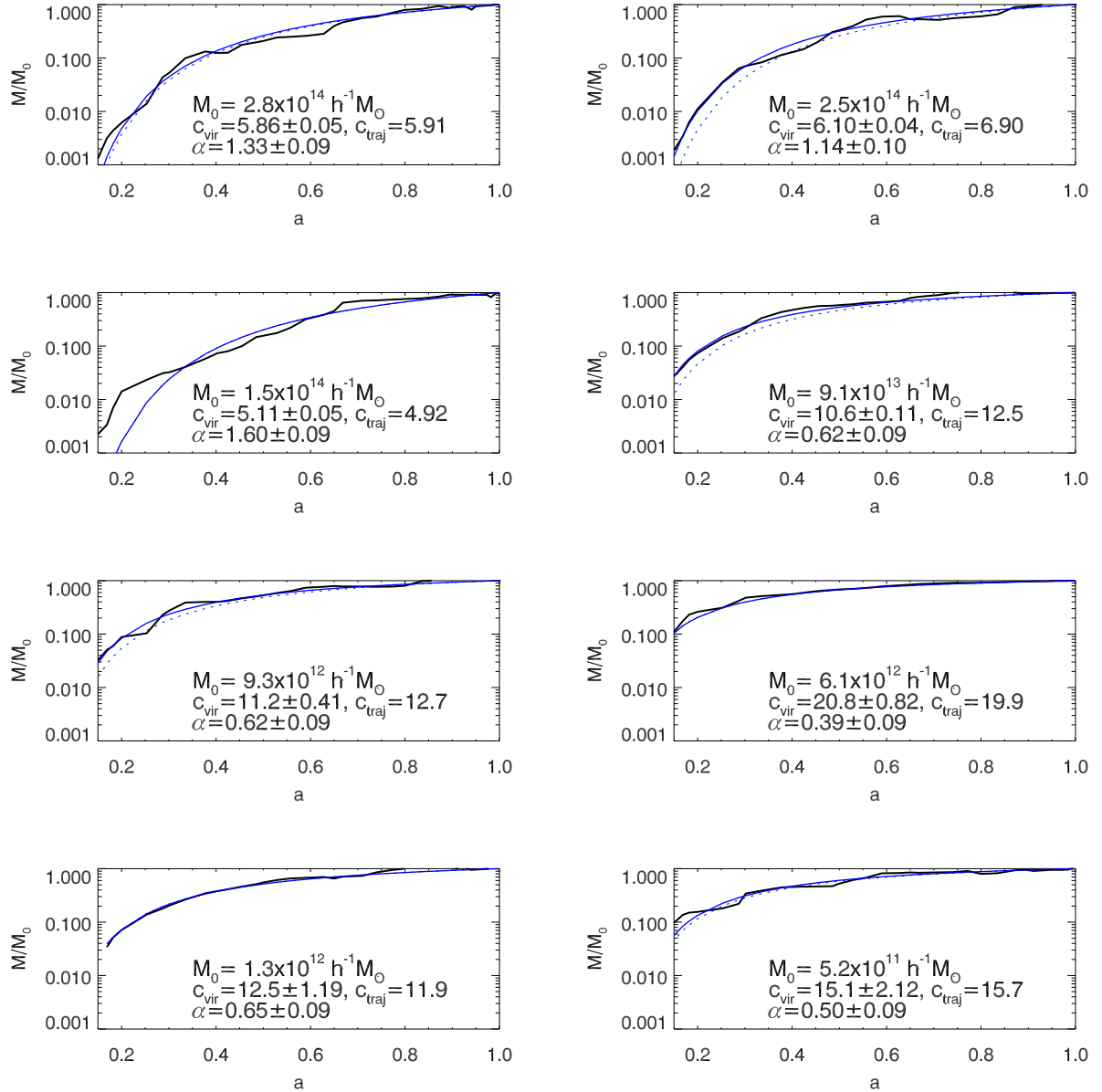


FIG. 3.— Selected mass accretion trajectories, showing the evolution of the most massive progenitor for individual halos in the simulation (thick). Functional fits to the growth curve of each halo using Eq. 3 are shown as thin smooth lines. The dotted lines represent the expected halo trajectory based on the value of the concentration parameter, using Eq. 3, with the value of a_c as derived by Eq. 7 using the value c_{vir} measured at $z = 0$ (and quoted in each panel). The quoted c_{traj} is derived by Eq. 7 using the a_c of the best fit to the actual growth curve.

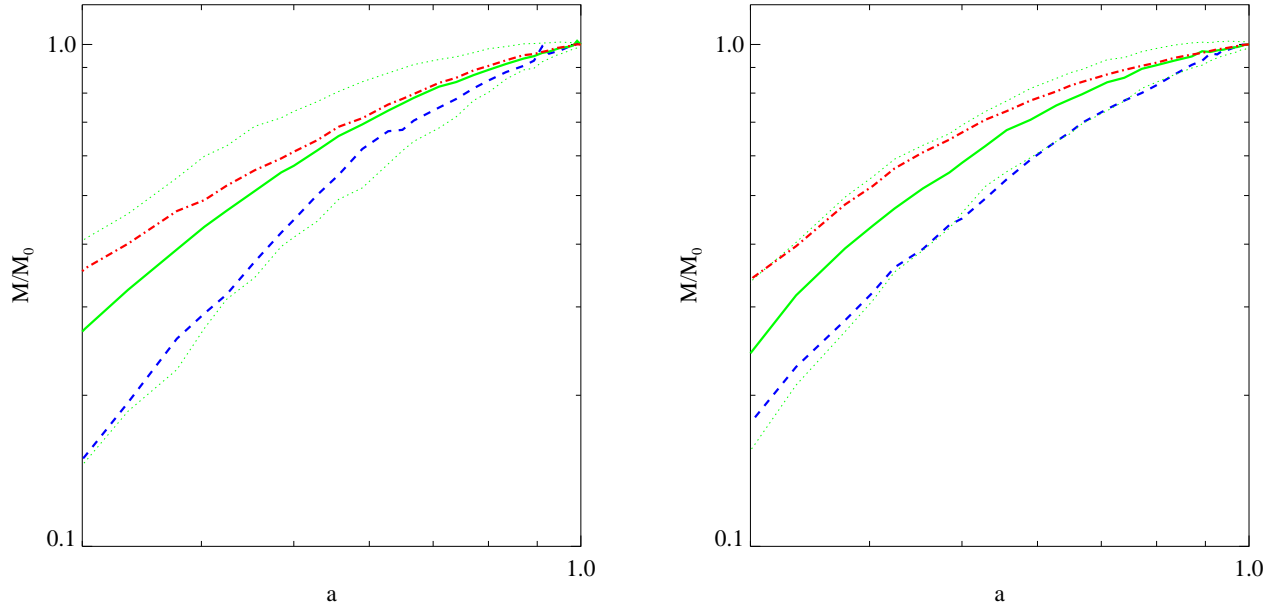


FIG. 4.— Average mass accretion histories, normalized at $a = 1$. **Left:** binned in 3 bins by final halo mass: $M_0 = 1 - 4 \times 10^{12} h^{-1} M_\odot$ (dot-dashed), $M_0 = .4 - 3 \times 10^{13} h^{-1} M_\odot$ (solid), and $M_0 > 3 \times 10^{13} h^{-1} M_\odot$ (dashed). The three (green) curves connect the averages of $M(a)/M_0$ at each output time. The pair of dotted lines shows the 68% spread about the middle case (the spread is comparable for the other bins). We see that massive halos tend to form later than lower mass halos, whose mass accretion rate peaks at an earlier time. **Right:** binned in 3 bins by formation epoch a_c . Dot-dashed lines correspond to early formers (typically low mass halos), dashed lines to late formers (typically higher mass halos). The averages and spread are displayed in analogy to the left panel.

the redshift dependence proposed for the NFW model fails to match accurately the dependence seen in simulations. Another shortcoming of this kind of definition is that it is limited to using the value of the halo trajectory at one time, which may introduce noise and miss relevant information. It would be useful to find a quantity which more fully characterizes the whole assembly history of the halo, and preferably one which does not depend on the redshift of observation z_o (at a possible cost that such a definition may be allowed to have formation times in the future).

By examining a range of full mass assembly histories for our sample of halos, we have found a useful parameterized form that captures many essential aspects of halo growth over time. Remarkably, we find that both average mass accretion histories and mass accretion histories for individual halos, as observed at $z = 0$, can be characterized by a simple function:

$$M(a) = M_o e^{-\alpha z}, \quad a = (1 + z)^{-1}. \quad (3)$$

Although individual halo trajectories may deviate from this form significantly in places (e.g., at the time of a major merger), this one-parameter model (in addition to the halos' final mass M_o) provides a remarkably good characterization of the range of halo mass accretion trajectories. Fits to this equation are shown in Figure 3 for several representative individual halos. van den Bosch (2001) has independently shown that a similar, two-parameter, functional form can be used to represent halo mass accretion histories for a variety of cosmologies and over a large mass range.

The single free parameter in the model, α , can be related to a characteristic epoch for formation, a_c , defined as the

expansion scale factor a when the logarithmic slope of the accretion rate, $d \log M / d \log a$, falls below some specified value, S . The functional form defined in Eq. 3 implies $a_c = \alpha / S$.

The same formation epoch can be defined equivalently for any “observing” epoch z_o of that halo, by replacing a in Eq. 3 by a/a_o . In this case, the characteristic formation time is related to α via

$$a_c = a_o \alpha / S. \quad (4)$$

Thus at any such observing redshift, with scalefactor $a_o = 1/(1 + z_o)$ and mass $M_o = M(z_o)$, the mass growth is fit by

$$M(a) = M_o \exp \left[-a_c S \left(\frac{a_o}{a} - 1 \right) \right]. \quad (5)$$

This implies that, for any halo whose mass accretion trajectory resembles Eq. 3, the characteristic formation time is the same regardless of the redshift z_o at which the halo is observed. In what follows we have chosen $S = 2$. Since the value of S is not used for the fit but only serves to define a_c , this choice is arbitrary.⁴

The range of formation scalefactors defined in this manner exhibits a log-normal distribution, whose mean value increases with increasing mass — low mass halos typically accrete their mass early, while high mass halos are typically still accreting mass rapidly in the present epoch. However, for a given mass, there is a large scatter in formation epoch. The scatter in the mass accretion trajectories for a given mass can be seen in Figure 4; we resume a detailed discussion of the mass dependence of a_c and the scatter about this relation in §7.

⁴ However, $S=2$ or something similar is required to match the B01 model behavior that we describe in §7.

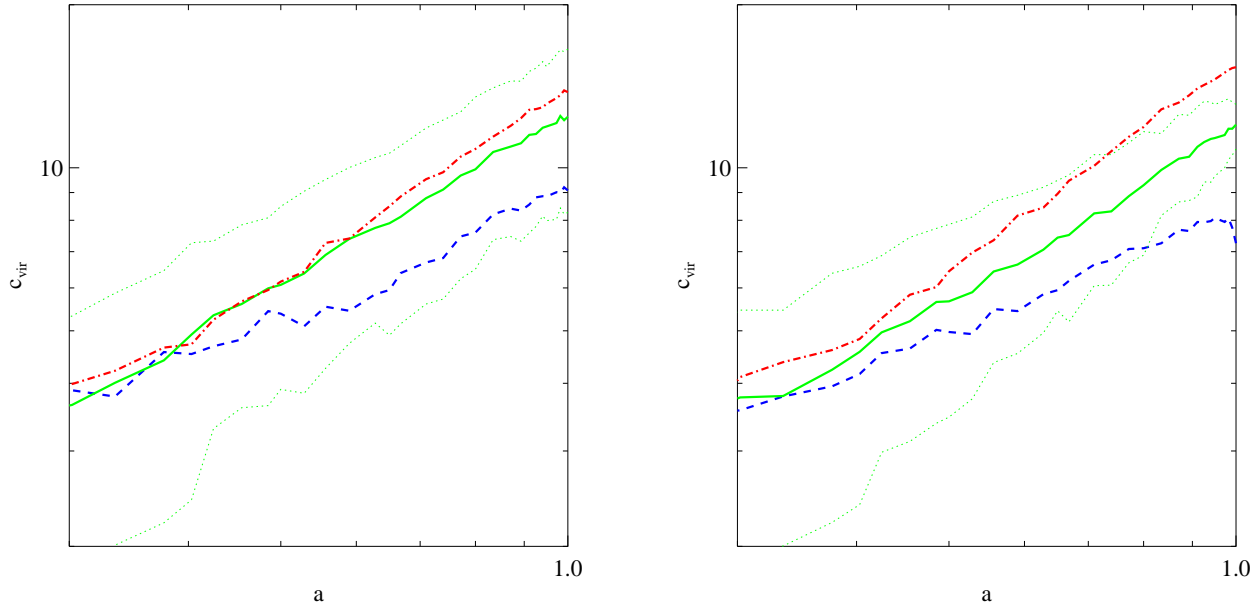


FIG. 5.— Average evolution of the concentration parameter. **Left:** binned by the final halo mass as in the left panel of Figure 4. We see that massive halos typically have lower, more slowly evolving c_{vir} values than low mass halos. **Right:** binned as a function of formation epoch as in the right panel of Figure 4.

5. CONCENTRATION AND ASSEMBLY HISTORY

We find that the concentration of a halo is tightly correlated with the characteristic formation epoch as defined in the above section. Figure 5 shows the average evolution of the concentration parameter for halos in different mass ranges, corresponding to the average mass trajectories shown in Figure 4. From this figure it is clear that halo concentrations have a stronger trend with less scatter when binned on a_c (right) than when binned on mass (left).⁵ We therefore investigate how c_{vir} is related to a_c directly.

Figure 6 shows the relation between concentration and a_c for halos at $z = 0$. The concentration of a halo is strongly correlated with its characteristic formation time, and a good fit is obtained with the inverse relation:

$$c_{\text{vir}} = c_1/a_c, \quad (6)$$

where $c_1 = 4.1$ is the typical concentration of halos forming today. The scatter about this relation is already not too large for all the halos, but we note that most outliers fall in one of the following three special categories:

1. the halo has a truncated trajectory that does not extend far back to the past, and thus a_c is not well determined;
2. the halo has a significant discontinuity in its c_{vir} trajectory at the final output time only, so that this value is not representative of the whole trajectory (this can occur if there is a merger or other disruption occurring at the final output time); or
3. the assembly history includes a merger that is substantially larger than the average accretion rate

at that time, and thus Eq. 3 does not provide a good description of the actual history.

To deal with special case (1), halos with trajectories which do not extend as far back as $z = 1$ are excluded from further analysis (fewer than 5% of cases; these halos are indicated by plus symbols in Figure 6). For case (2), outlined by squares in Figure 6, we find that a much better agreement with the median relation is obtained when the last discrepant value of c_{vir} is replaced by the value of c_{vir} in the preceding output time. We do not attempt to cure the problem associated with case (3), except for keeping in mind that the outliers remaining in the $c_{\text{vir}}-a_c$ relation are often due to a failure of Eq. 3 to adequately model the history of that halo. With these modifications, the scatter in c_{vir} for a given a_c is $\Delta(\log c_{\text{vir}}) \approx 0.09$, without removing additional scatter due to large NFW fit errors (see also Figure 9), and $\Delta(\log c_{\text{vir}}) \approx 0.05 - 06$ when errors in c_{vir} are corrected for.

We have also examined the dependence of c_{vir} on the merger history of halos, which is correlated with but distinct from the mass accretion history of the most massive progenitor discussed above. Since halos that did not undergo a recent major merger are more likely to have accreted most of their mass early, they typically have earlier formation times and higher concentration values (see Figure 17). However, we find that the parameter a_c we have defined based on the mass assembly history is more useful; for halos with a given a_c value, the occurrence of a recent merger is not an important factor affecting the concentration. This can be seen in Figure 6, which demonstrates that halos which have experienced recent major mergers (circles; defined here as a merger ratio of greater than 1/3)

⁵ Note that the figure only shows this directly for $z = 0$, although it is true at any redshift z_0 when a_c is measured at z_0 . However, the scatter about the average trajectory increases with z , since a halo can't uniquely predict its future.

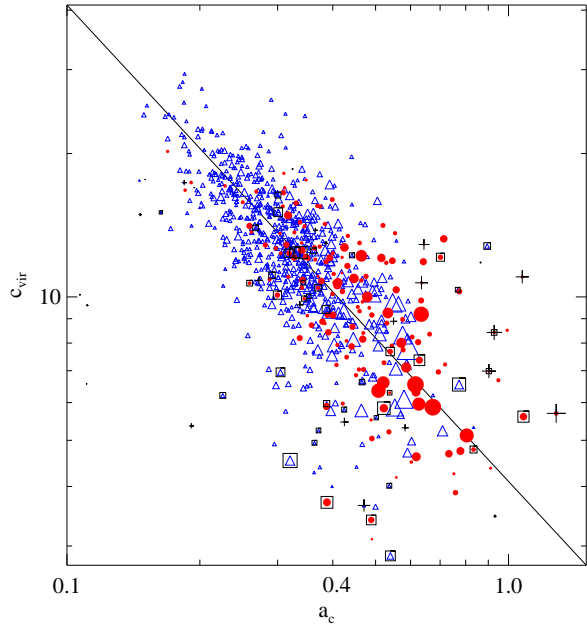


FIG. 6.— Concentration versus formation epoch for halos more massive than $10^{12}h^{-1}M_{\odot}$ at $z=0$. Halos that had major mergers ($M_2 \geq M_1/3$) since $z=1$ are indicated with filled circles, halos that did not have major mergers since $z=1$ are shown with open triangles. The size of the points is inversely proportional to the error on the points (in both c_{vir} and a_c). Halos with short trajectories are marked with pluses and excluded from further analysis; halos whose final c_{vir} value jumps are outlines with squares and treated as described in the text.

form later on average but follow the same trend in c_{vir} vs. a_c (albeit with more scatter; see §9) as halos with no recent major mergers (triangles).

6. DEPENDENCE ON REDSHIFT OF MEASUREMENT

We now investigate how the correlation found in the previous section between c_{vir} and a_c as measured at $z=0$ behaves as a function of the redshift z_o . We found that c_{vir} is inversely proportional to a_c , or equivalently to the fit parameter α from Eq. 3. If the determining factor in a halo’s concentration is the shape of its mass growth curve then we expect that a similar dependence would hold for all redshifts. Eq. 4 would then imply that the concentration should be inversely proportional to a_c/a_o for any a_o when the halo is observed. In Figure 7, the measured concentration values are plotted vs. this scaled formation epoch for halos at $z_o = 0, 1$, and 2 . Halos appear to follow the same trend regardless of mass or redshift.

In order to obtain the most reliable estimate of the proportionality constant c_1 in the linear regression of c_{vir} and a_c/a_o , we use halos in the mass range $1 - 5 \times 10^{12}h^{-1}M_{\odot}$, and consider the errors in both a_c and c_{vir} while excluding outlying points that are more than $2\text{-}\sigma$ away from the best fit line. Considering halos at $z_o = 0, 1$, and 2 together yields the same result as obtained for z_o halos alone, properly scaled by a_o :

$$c_{\text{vir}} = c_1 a_o / a_c, \quad (7)$$

where $c_1 = 8.2/S$ (here we have used $S = 2 \rightarrow c_1 = 4.1$.) As before, the parameter c_1 is the typical concentration

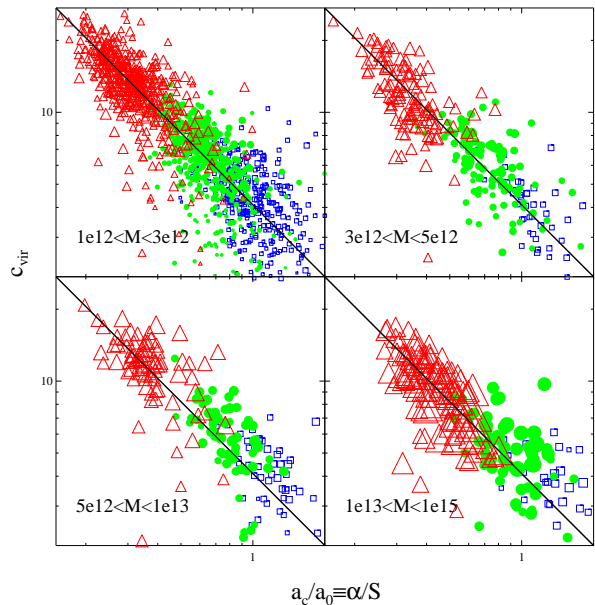


FIG. 7.— Concentration versus scaled formation epoch a_c/a_o , for halos at $z=0$ (triangles), $z=1$ (circles), and $z=2$ (squares). The 4 panels correspond to different mass ranges. At all masses and redshifts, the concentration parameter c_{vir} is well fit by the functional form $c_{\text{vir}} = c_1 a_c / a_o$, where $c_1 \sim 4.1$ (represented by the solid line in each panel).

of halos whose formation time is at the time of measurement, $a_c = a_o$. For the Λ CDM cosmology considered here, and $a_o = 1$, this is the typical concentration of halos of $\sim 7 \times 10^{13}h^{-1}M_{\odot}$. Figure 7 shows that this formula provides a good description of the observed correlation between concentration and formation time for halos at all masses and redshifts.

7. PROPERTIES OF THE FORMATION TIME

As discussed above, B01 showed that the average concentration value measured for halos of a fixed mass scales as $c_{\text{vir}} \propto a_o$. This trend was understood using a simple model in which the central densities of halos are set by the density of the universe at a characteristic collapse time, \tilde{a}_c , implying $c_{\text{vir}} \propto a_o / \tilde{a}_c$. Crucial to the success of this model was that the definition of collapse time, \tilde{a}_c , was independent of a for fixed mass halos. In the previous sections we showed that a similar result obtains using a different definition of the characteristic formation time: $c_{\text{vir}} \propto a_o / a_c$, where a_c is derived based on the actual history of mass accretion in individual halos, rather than on a simple universal scaling argument as in B01. In order to obtain a consistent trend with redshift, we expect that a_c (like \tilde{a}_c) will be independent of the epoch z_o when the measurement is performed for a given halo mass. This assumption is tested in Figure 8, which shows the dependence of a_c on mass, for halos identified at three distinct redshifts in the simulation. Within the errors, it shows roughly the same mass trend regardless of redshift; this is a key feature that our a_c parameter has in common with

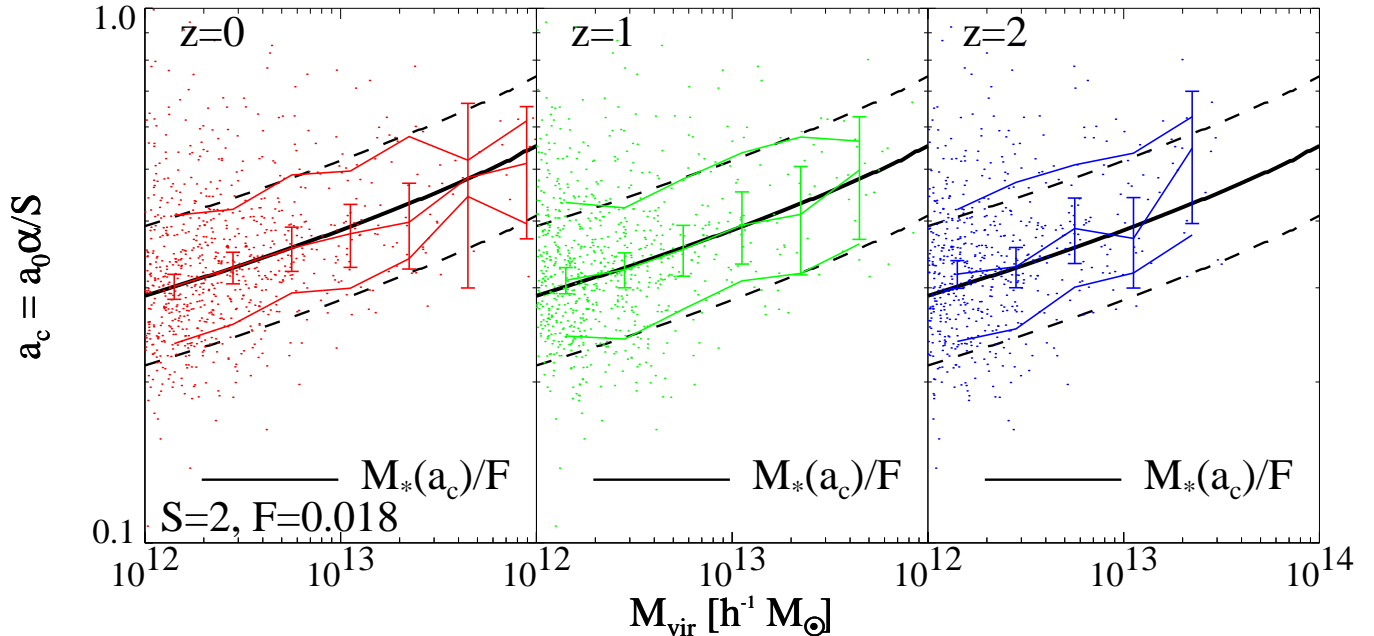


FIG. 8.— Mass dependence of a_c , shown for halos at redshifts $z = 0, 1$, and 2 . Dots represent individual halos. The middle thin lines with Poisson error bars indicate median values for the mass bins, and the outer thin lines indicate the 68 % scatter about the median. In each panel, the thick solid line is \tilde{a}_c as a function of mass from the model of B01 and the thick dashed lines indicate the scatter about this value needed to account for the 35% measured scatter in concentration.

the collapse epoch \tilde{a}_c defined by B01. In fact, these parameters can be directly associated (for an appropriately chosen value of S). For example, we find that \tilde{a}_c follows the same mass trend as our derived a_c (with $S = 2$) if it is defined as in B01 ($M_*(a_c) = FM$) with $F = 0.015$.

The value of a_c for a given mass halo also shows significant scatter, as can be seen in Figure 8. The amount of scatter (~ 0.13 in the log) can almost completely account for the scatter seen in the c_{vir} vs. M relation (discussed in detail in §9). Figure 9 shows probability distributions of a_c and c_{vir} for a given mass range. The intrinsic scatter in c_{vir} for a given a_c is relatively small compared to the scatter in c_{vir} for a given mass, and we find that the measured distribution of c_{vir} can be practically reproduced if Eq. 7 is used to transform each measured a_c value into a concentration. Thus the scatter in concentration can be understood as deriving almost exclusively from the range of accretion histories for a given halo mass.

It is encouraging that our definition of formation time is robust both in terms of measuring the same value at different epochs along the growth curve of a given halo, and in terms of its average value, for halos of a given mass when measured at different redshifts. We explore this further in the next section. Although a given halo mass accretion history that is a perfect fit to Eq. 3 will have a constant value of a_c regardless of when it is observed, we find that *the early part of a halo's trajectory is not a good indicator of the latter part*. This is shown in Figure 10, which demonstrates that the formation time measured using the first half of a halo's history is not correlated with the formation time measured using the second half.

We have demonstrated that the tight correlation found in the simulations between a_c and c_{vir} can account for the mass and redshift trends and the scatter in $c_{\text{vir}}(M)$. However, it would be useful to have a way to model the concentrations without such a computationally expensive simulation, for incorporation into analytic or semi-analytic models. Of course, the model of B01 did this to some extent for *average* halo properties as a function of mass and redshift, but this neglects the tight correlation found here between *individual* halo density profiles and their mass accretion histories. In this section we compare the mass accretion trajectories from our simulation with trajectories generated using the EPS formalism and test whether the correlation we found, $c_{\text{vir}} \propto a_c^{-1}$, can be used to predict concentrations for *individual* halos semi-analytically.

Comparisons of specific aspects of mass accretion histories as derived semi-analytically and as extracted from simulations have been performed (SLKD; Gardner 2001), but here we focus on the quantity relevant for our modeling of c_{vir} , namely the range of values of $a_c(M, z)$, which has not been investigated previously. There are essentially four relevant questions in this analysis:

- do EPS trees produce the same range of a_c values for a given mass as halo trees extracted from simulations?
- do EPS trees produce the same trend of a_c with M , which could then explain the trend of c_{vir} with M ?
- is $a_c(M)$ constant with redshift for EPS trees, which could then explain the $c_{\text{vir}}(z)$ trend?

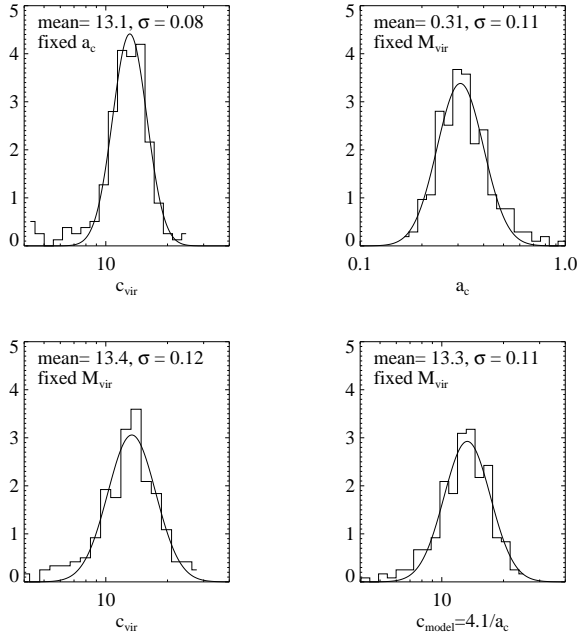


FIG. 9.— Probability distributions of a_c and c_{vir} when other parameters are fixed. **Top left:** the distribution of c_{vir} for a given value of a_c ; the scatter is less than $\sim 20\%$ (with no correction for fit errors in c_{vir} or a_c), and less than $\sim 15\%$ when corrected for errors in c_{vir} . **Top right:** the distribution of a_c for halos in the mass range $1.5 - 2.5 \times 10^{12} h^{-1} M_\odot$. **Bottom left:** the distribution of c_{vir} for halos in the same mass range. **Bottom right:** the distribution of c_{vir} for the same mass range, as predicted from a_c via Eq. 7. The mean and scatter of each distribution is listed at the top of the panel and is virtually equivalent between the modeled c_{vir} (bottom right) and the measured simulation values (bottom left).

- does the scatter in a_c for a given mass in EPS trees account for the scatter in the measured $c_{\text{vir}}(M)$ relation?

8.1. a_c vs M_{vir} and the EPS Offset

In order to answer these questions, we first generate a random ensemble of mass accretion histories. This is done by coupling the extended Press-Schechter formalism, which predicts the probability of accreting a given mass in a given time, with a method for generating Monte-Carlo merger trees. Here we use the scheme introduced by SK99, with an additional modification proposed by Bullock, Kravtsov, & Weinberg (2000). For completeness, we outline the fundamental aspects of the method in Appendix C.

We consider the list of all halos found in the simulation with masses larger than the minimum-fit mass $2 \times 10^{11} h^{-1} M_\odot$ (~ 3000 halos). We then generate ten Monte-Carlo realizations of mass accretion trajectories for each of these halos, based solely on its $z = 0$ mass, keeping track of the growth of the most massive progenitor as a function of time. We start at $z = 0$ and trace histories back to $z = 7.2$. Using this most massive progenitor trajectory, α is calculated by fitting the trajectory to Eq. 3. The value of a_c is then defined by Eq. 4, with $S = 2$.

Figure 11 shows the distribution of a_c values found for different given mass ranges, for both the simulated halo trajectories and the EPS trajectories. We see that the distribution of a_c values from EPS trees is systematically

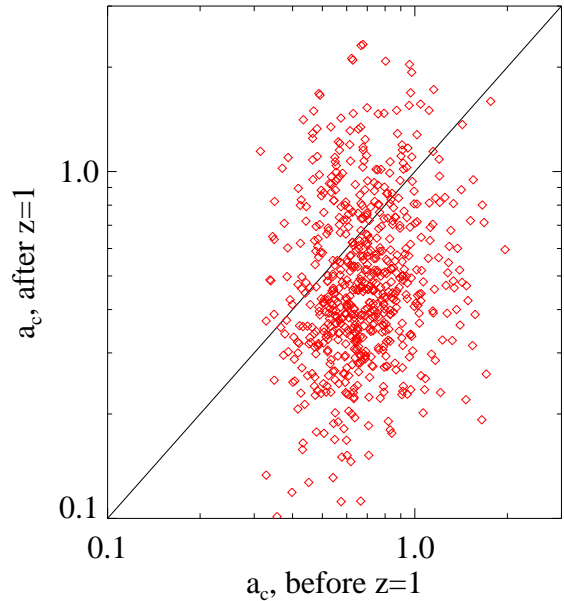


FIG. 10.— Comparison of the formation epoch a_c as measured using the trajectory to $z = 1$ and the trajectory after $z = 1$. Either of these values individually is well correlated with the standard value using the whole history (i.e., on average a_c stays constant for a given trajectory), but they are not clearly correlated with each other, indicating that a halo’s past does not predict its future. Note that the vertical scatter is larger than the horizontal scatter, reflecting the fact that the second half of the trajectory does not constrain the value of a_c very well because this is the shallow part of the function.

offset toward later formation times for all mass ranges, and also appear to be slightly broader. A similar discrepancy was found by SLKD, although they did not investigate the same quantity — they found the average mass of the largest progenitor to be larger in the EPS trees than in the simulated trees at low redshift, and smaller at high redshift. This implies later formation times for the simulated halos, as seen here. This discrepancy can be understood in terms of comparing the conditional progenitor mass functions; SLKD showed that EPS over-predicts it for low masses and under-predicts it for high masses, with the mass scale of the crossover decreasing with increasing redshift. This discrepancy in formation epochs seems to directly reflect the more well-known finding that PS over-predicts the number density of halos below M_* and under-predicts the number density above M_* (e.g., Gross et al. 1998; Sheth & Tormen 1999). Although only one cosmological model (Λ CDM) has been investigated here, the disagreement of the halo mass function with Press-Schechter is generic and we expect that the formation time discrepancy would be seen to some extent in any CDM cosmogony.

Although we find a discrepancy in the median a_c values as a function of mass, we find that they are offset by a constant multiplicative factor. Figure 12 shows the median and 68% scatter for $a_c(M)$, from the EPS trajectories and the simulated trajectories, for $z = 0$ halos. The constant offset is in the sense that the characteristic formation

epochs derived from the EPS trajectories are roughly 25% larger than those measured from the simulation trees. The scatter is quite comparable, though it is slightly larger for

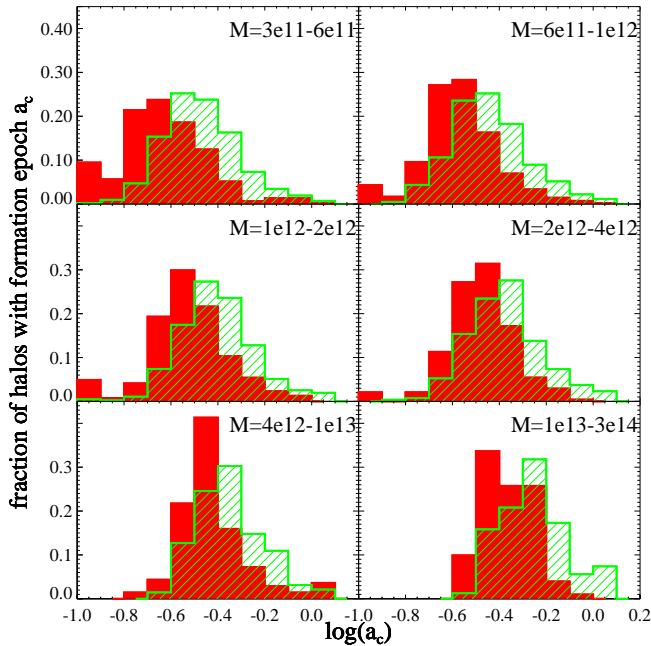


FIG. 11.— Comparison of a_c values in the simulation with those derived from EPS trees, for various mass ranges in the different panels. The filled histogram represents simulated halos and the shaded histogram represents ten realizations of EPS trajectories for the same set of masses. Abnormal halos (whose trajectories end prematurely) in the simulations are counted in the left-most bin; the number of these cases is small, and negligible above $10^{12}h^{-1}M_\odot$.

the EPS-derived values.

If we assume that the a_c values found using EPS trajectories are correct except for this constant 25% offset, due to the known discrepancies in PS theory, then these values can be used in combination with Eq. 7 to estimate c_{vir} for each halo, using its EPS-derived trajectory. Figure 13 shows the measured $c_{\text{vir}}(M_{\text{vir}})$ for simulated halos at $z = 0$, compared with the c_{vir} value obtained using this semi-analytic method. The constant c_1 has been shifted by a factor of 1.25, but otherwise we are able to match both the mass trend and the scatter of the measured c_{vir} values in the simulation with this simple model.

8.2. Redshift Dependence in EPS

We can also test whether the redshift dependence of the EPS trajectories is consistent with our model, and with the c_{vir} trend seen in the simulation. B01 showed that for a given mass, $c_{\text{vir}} \propto a$, implying, for our model, that (on average) a_c must be uniquely set by the mass, independent of redshift. Figure 14 shows the $a_c(M)$ relation at redshifts $z = 0, 1, 2$, and 3, using one realization of EPS trajectories (again, with the mass weighting of the simulated halos). There is no discernible change in the median or scatter over the entire mass range examined. Using Eq. 7 to translate these values into predicted c_{vir} values will thus result in exactly the trend found by B01, i.e., that $c_{\text{vir}} \propto a$, with the correct mass trend and scatter for all redshifts.

Given the fact that the a_c values are robust to changes in z_0 , it might be considered somewhat puzzling that

the $a_c(M)$ relation remains constant with redshift, since clearly the halo masses are significantly lower at high redshift. Naively, one might think that since the masses shift, the average halo of a given mass would have a higher a_c value in the past. However, for a given mass halo at $z = 0$, those halos which have the latest formation times will have the smallest masses at high redshift, and those which form earliest will have the highest mass at high redshift. When halos are combined with the proper mass weighting, they thus conspire to keep the same relation regardless of redshift. Figure 15 demonstrates this in detail. In the upper panel, the $a_c(M)$ trend is shown at $z = 0$ for halos in two distinct mass ranges. In the lower panel, these same halos are shown at $z = 3$: the a_c values for each halo remain essentially unchanged, but they are now plotted against their $z = 3$ masses. Halos in any given mass range at $z = 3$ consist of a combination number of low a_c halos that will have low $z = 0$ masses and high a_c halos that will have high $z = 0$ masses. These add in a manner that maintains the shape and normalization of $a_c(M)$. The fact that $a_c(M)$ is constant with redshift is an indication that the model proposed by B01 is a reasonable one — i.e., that (on average) the formation time of a halo is set only by its mass, and can be related to the time that mass was a fixed fraction of M_* .

In summary, the formation times of halos in EPS (using an improved version of the SK99 method to generate merger trees) are somewhat later than those found in the ART simulation. However, if we measure a_c values for these semi-analytic trajectories (using Eq. 5), multiply these values by a constant factor (0.8), and translate these formation epochs to concentrations using the relation $c_{\text{vir}} = c_1 a_0 / a_c$, we are able, to a good approximation, to match the scatter, mass, and redshift dependence of the c_{vir} values found for simulated halos. This method can be used in semi-analytic models to estimate halo concentrations that are both based on their individual mass growth histories and have the correct distribution at every redshift.

The only disadvantage of the above method is that it requires generating full mass accretion histories for a sample of halos. Since Eq. 5 is a one-parameter model, one might be tempted to directly calculate the more prevalent formation redshift $z_{f0.5}$, when the most massive progenitor mass was half of M_0 , and whose probability distribution can be calculated directly from EPS without generating merger trees, and then translate this value into z_c using Eq. 5 in order to derive a concentration. However, while this method predicts the mean values relatively well, in fact there is substantially more scatter in values of $z_{f0.5}$ than in values of z_c . This is due to the fact that individual trajectories are noisy, and at any one point in the trajectory, there is likely to be significantly more scatter than in the shape of the halo as a whole.

9. SCATTER IN THE $c_{\text{vir}}(M_{\text{vir}})$ RELATION

9.1. Evaluating a Corrected Scatter

The scatter in the concentration parameter has been estimated by B01 and Jing (2000), and it may have a number of important observational implications. Jing (2000) found a scatter of 0.08 – 0.1 in $\log_{10} c_{\text{vir}}$, while B01 de-

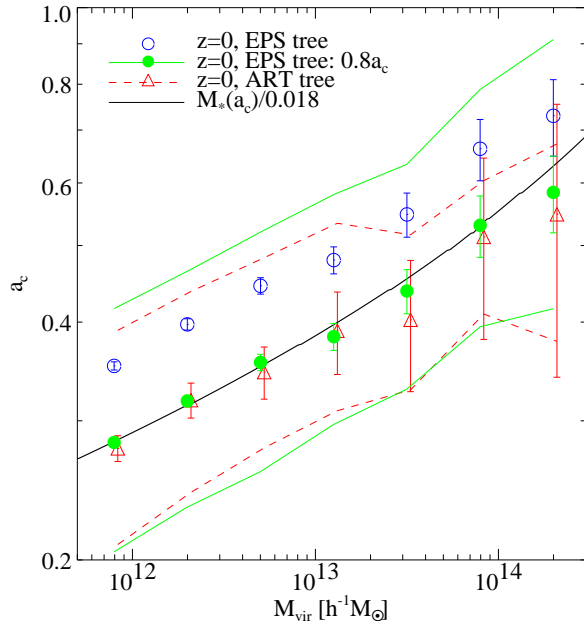


FIG. 12.— Comparison of the median $a_c(M)$ relation with that derived from EPS trees. The triangles correspond to the trees from the ART simulation. The open circles represent ten Monte-Carlo realizations of EPS merger trees for each simulated halo mass. The EPS-derived a_c values are offset about 25% higher than those measured in the simulation. The filled circles are the EPS results shifted down by 20%. In each case the error bars are Poisson based on the number in the mass bin. The outer lines represent the 68% scatter about the median relation. The dark solid line in the middle represents the model of B01 with $F=0.015$, and 35% scatter about that model.

rived a somewhat larger scatter of $\Delta \log_{10} c_{\text{vir}} = 0.14$.⁵ A revised scatter estimate from our improved halo catalogs, which also relies on the mass trajectories, is presented here. We also discuss how the scatter in c_{vir} is affected by the merging history of halos.

B01 devised a method for correcting the scatter estimate for errors in the fits, and actually plotted this corrected scatter in Figure 4. Our new halo catalogs have significantly fewer halos with large fit errors, and thus a smaller uncorrected scatter, but encouragingly, when we use the method of B01 for correcting this for fit errors and Poisson errors, we get almost identical results (shown in Figure 16). This method involves doing 500 Monte Carlo realizations of each halo, in which their c_{vir} value is chosen from a one-sided Gaussian deviate with a standard deviation error on the measured c_{vir} value. This value is then added or subtracted to the measured value depending on whether the measured value was below or above the median value for that mass. Poisson errors due to finite statistics are then subtracted in quadrature to obtain an estimate for the intrinsic scatter — which we also find to be $\Delta(\log c_{\text{vir}}) \approx 0.14$.

As mentioned previously, there may be halos which for a short period of time are not well-fit by an NFW density profile; in many cases this occurs when a halo is undergoing merging or disruption. In most cases, this results

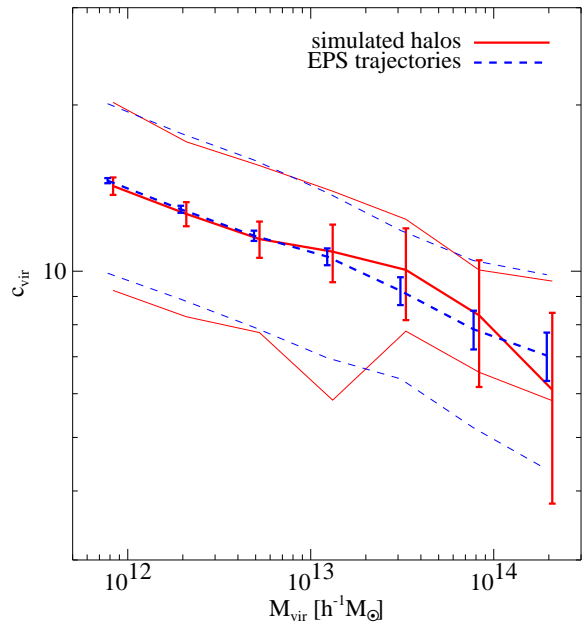


FIG. 13.— Comparison of the median $c_{\text{vir}}(M)$ relation for simulated halos (solid lines) with those obtained using Eq. 7 and the a_c values derived from EPS trajectories (dashed lines). As in Fig. 12, the EPS a_c values have been offset 20% lower. Ten Monte-Carlo merger tree realizations are generated for each simulated halo mass. Some selected realizations look virtually identical to the distribution for simulated halos. The outer pair of thin lines represent the corresponding 68% scatter and error bars are Poisson based on the number of halos in each bin.

in an artificially low value of c_{vir} , which usually persists only for one timestep. In order to remove the effects of badly estimated concentration parameters which persist only for a short time, we use the merging history of a halo to identify those cases where the concentration has jumped significantly since the previous output time. The $c_{\text{vir}}(M)$ relation excluding these halos (which make up $\sim 8\%$ of the total) is plotted in Figure 16, compared to the whole sample; the scatter for this sample is reduced from $\sim 38\%$ to $\sim 31\%$. Note that the exclusion of these halos does not change the median value significantly. We regard the scatter estimate from excluding these halos as a lower limit. With this correction, our analysis is closer to the scatter estimate presented by Jing (2000). It is possible that some of the remaining discrepancy could be due to an underestimate of fit errors; the total scatter for the very massive halos in our analysis is slightly smaller. However, it should also be pointed out that Jing (2000) only considered relaxed halos, and our analysis contains halos with a full range of properties, including those that have been recently disrupted — and these add significantly to the scatter.

9.2. Scatter and Halo Merger History

As discussed in §5, halos with recent major mergers display the same trend between concentration and a_c (Eq. 3), but with somewhat more scatter. We show in Fig-

⁵ The value of 0.18 reported in the abstract of B01 was actually the directly measured scatter, without any correction for fit errors. The corrected value of 0.14 is illustrated in B01 Figure 4. This footnote is aimed at correcting this oversight in that paper.

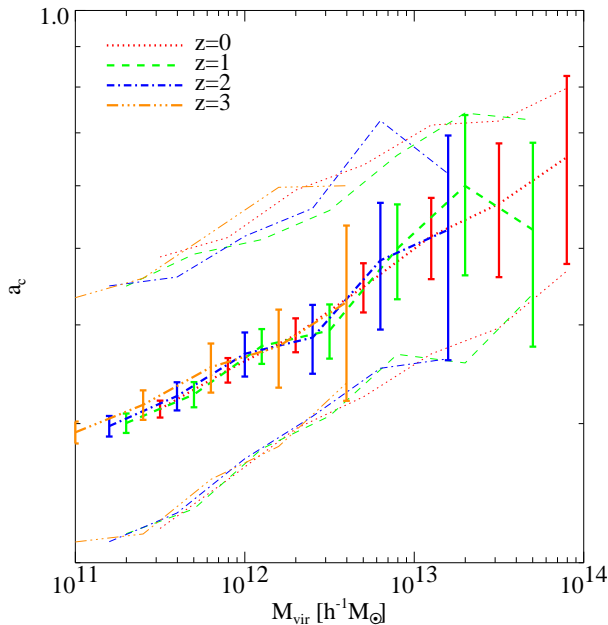


FIG. 14.— Robustness of $a_c(M)$ to the redshift of “observation” in one realization of an EPS tree. The 4 different sets of curves and symbols refer to 4 different redshifts. The thick lines represent the median a_c values and the pairs of outer thin lines represent 68% scatter. Error bars represent Poisson error based on the number in each mass bin. As predicted by Eq. 3, the median a_c value is uniquely determined by the halo mass, independently of the redshift.

ure 17 that these halos also follow the same basic trend with mass. This figure compares this trend and scatter in $c_{\text{vir}}(M)$ for all halos with that seen in halos that have not had a major merger since $z = 2$. The scatter is reduced from about 31(38)% for all halos to $\sim 26(28)\%$ for those halos without recent major mergers, where the first listed estimate is when halos with large c_{vir} jumps are excluded, and the number in parenthesis includes all halos. (The implied correction for halos without recent mergers is not large since most of the halos with jumps are in the process of merging.) The sample of halos which *have* had a major merger since $z = 2$ do not have reduced scatter compared to the whole sample. Since halos with recent major mergers have later formation times on average, when they are excluded from the sample, the remaining halos have higher c_{vir} values by a factor of about $\sim 10\%$ compared to the complete sample; this can also be seen in Figure 17.

The amount of scatter in the concentration parameter for a given mass is of particular interest because of its possible implications for scatter in the Tully-Fisher relation (see, e.g., B01; van den Bosch 2000), and there is particular interest in the amount of scatter in the concentrations of spiral galaxies. In many scenarios for galaxy formation, major mergers destroy disks, and thus halos with recent major mergers are unlikely to host spiral galaxies. As described above, not counting these halos reduces the scatter of the whole sample and thus may reduce consequential scatter in Tully-Fisher to a level that can be matched with observations. Whether these remaining halos host spiral

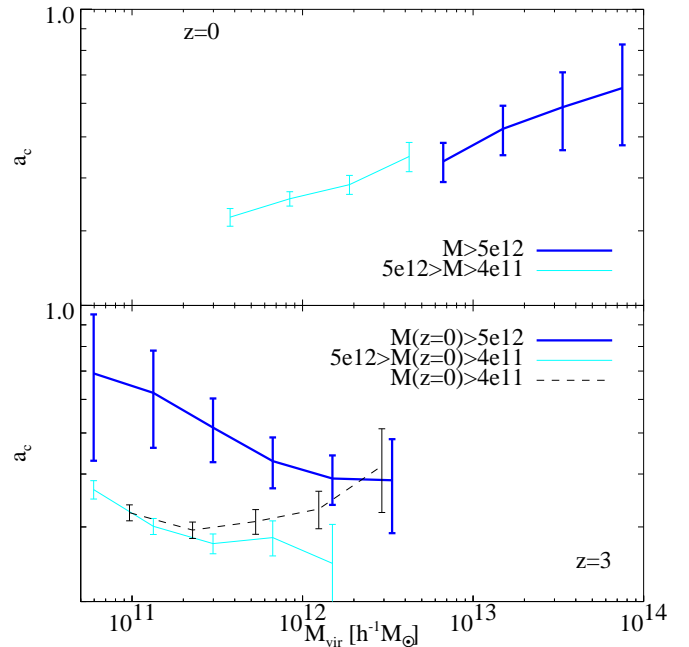


FIG. 15.— An analysis of the robustness of $a_c(M)$ to redshift, in EPS trajectories. **Top:** $a_c(M)$ at $z = 0$, broken into two mass ranges. **Bottom:** $a_c(M)$ at $z = 3$ for the same mass ranges determined at $z = 0$ (dark thick: high mass; light thin: low mass). The ratio $M(z=3)/M(z=0)$ is related to a_c , such that for a given $z = 0$ mass, halos with high a_c will have lower $z = 3$ masses. The dashed line shows the sum of the mass bins, which follows a similar trend with mass as the $z = 0$ halos. The apparent upturn in the left-most bin of the dashed curve is due to the exclusion of halos less massive than $4 \times 10^{11} h^{-1} M_{\odot}$ at $z = 0$, which contribute lower a_c values.

galaxies may be influenced by how much mass they have accreted since their last disruption; this could bring the concentrations of halos hosting spiral galaxies lower than the median shown here. It should also be noted that in this analysis we have only considered distinct halos. To get a full estimate of scatter and normalization for galactic halos we would have to include subhalos in the analysis, which B01 have shown have somewhat larger scatter in c_{vir} . We defer a full analysis of these issues to a later work.

10. DISCUSSION AND CONCLUSIONS

Making use of a large sample of dark halos simulated in a cosmological volume, we have studied the relation between mass accretion history and the density concentration of halos. Remarkably, halo mass growth curves (normalized to the final halo mass) can be accurately described by a one parameter function, in which mass accretion occurs rapidly at early times, and slows at late times. The characteristic “formation” time, a_c , defined as the time when the log-mass infall rate drops below a fixed value, fully defines the trajectory. We find that the value of a_c for each halo trajectory is independent of the epoch at which the halo is observed, a_o . In addition, the average value of a_c for halos of fixed mass is independent of redshift.

The NFW halo concentration parameter, c_{vir} , which, in combination with the halo mass, uniquely sets the shape of the density profile, is tightly related to a_c via $c_{\text{vir}} = c_1 a_o / a_c$. The central density of a halo at fixed radius grows rapidly when the mass accretion rate is high,

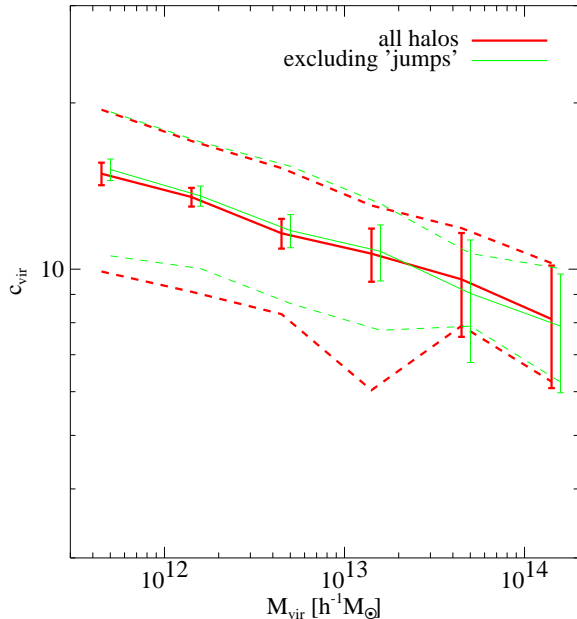


FIG. 16.— Scatter in the $c_{\text{vir}}-M_{\text{vir}}$ relation for halos at $z = 0$. The thick lines represent all the halos. The thin lines represent all halos whose concentration has not jumped by more than a factor of two (in either direction) since the previous output time (at $z = 0.01$). In each case, the solid lines represent the median value of c_{vir} , plotted with Poisson error bars, and the dashed lines represent the scatter corrected for errors in the individual profile fits and for Poisson scatter in the bins. In the mass range where the results are most reliable ($\sim 1 \times 10^{12} h^{-1} M_{\odot}$), the value of the corrected scatter in these two samples is $\Delta(\log c_{\text{vir}}) \approx 0.14$ and 0.12 , respectively.

and approaches a constant value as the mass accretion slows. This result is consistent with a picture in which the mass accretion rate determines how far accreted mass makes it into the center of a halo: for high mass accretion rates, accreted material makes it far into the center of the halo, but as it slows new material builds up on the outside. Thus central densities of halos asymptote to a value which is proportional to the density of the universe at the time when the mass accretion rate slows. In late forming halos this process is delayed and thus the final central density is lower. To demonstrate the model, in Figure 18 we plot the evolution of several variables for an early and late forming halo: the mass, concentration, log-slope of the mass accretion rate, scale radius R_s , and the density within a fixed radius. Each parameter is calculated analytically; this is done using Eq. 1, which specifies the density profile, Eq. 5, which specifies the mass accretion history, and Eq. 7, which specifies the relationship between them.

We showed that scatter in c_{vir} for a given mass can be explained almost exclusively by scatter in a_c for halos of that mass. Thus this model, based on the $c_{\text{vir}}-a_c$ correlation, captures successfully the main properties of the concentration parameter, including its mass dependence, redshift trend, and the scatter about these relations.

The formation times derived from semi-analytic realizations of EPS mass accretion histories were compared with those measured in the N-body simulation, and found to be systematically larger by 25%. This offset reflects known inaccuracies in the Press-Schechter approximation.

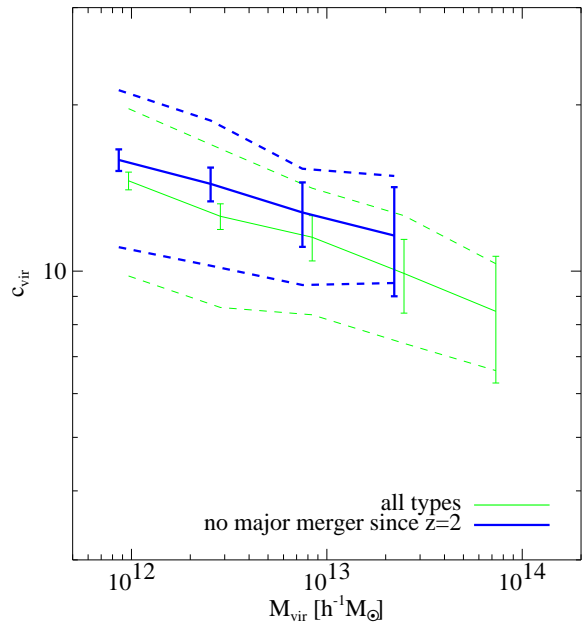


FIG. 17.— Type dependence of the $c_{\text{vir}}-M_{\text{vir}}$ relation for halos at $z = 0$. The thick lines represent halos which have not had a major merger since $z = 2$; the thin lines represent all types. In each case halos with big ‘jumps’ in c_{vir} are excluded, as described in the previous caption. In each case, solid lines represent the median value of c_{vir} , plotted with Poisson error bars, and dashed lines represent the intrinsic corrected scatter. For halos without recent mergers, the scatter is reduced to $\Delta(\log c_{\text{vir}}) \approx 0.10$.

By adjusting the formation times for this offset, we have successfully used the $c_{\text{vir}}-a_c$ correlation to reproduce the mass and redshift dependence of c_{vir} , and the scatter about these relations, using mass accretion histories derived from EPS. This technique is likely to be very useful for inclusion in semi-analytic models of galaxy formation, which so far have at best drawn c_{vir} randomly from an assumed global probability distribution, with no dependence on the halo’s history.

We have presented an estimate for the scatter in c_{vir} , with preliminary hints for how this scatter may depend on galaxy type. For halos of a given mass that have not had a major merger, we estimate that the scatter is as low as $\Delta(\log c_{\text{vir}}) \approx 0.1$. This scatter is roughly consistent with the scatter observed in the Tully-Fisher relation. However, we have not included subhalos in this estimate, so our results only apply to isolated field galaxies; including subhalos may increase the scatter. It is also interesting that such halos (those without recent major mergers, which could conceivably host disk galaxies) are also somewhat more concentrated, which is perhaps contrary to naive expectations.

It is worth pointing out that this is not the only attempt to connect the full mass accretion history of halos to their density structure. For example, Avila-Reese, Firmani, & Hernández (1998), building on the work of Zaroubi & Hoffman (1993), used an analytic approach based on shell-by-shell mass accretion to connect halo structure with mass accretion (see also Ryden & Gunn 1987). Although their

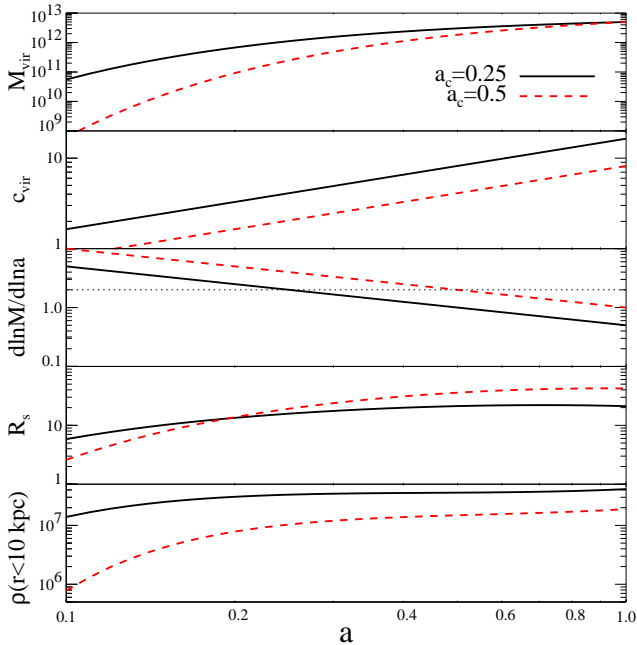


FIG. 18.— Evolution of mass and structure of two halos. From top to bottom, we plot the evolution of the mass M_{vir} , the concentration c_{vir} , the log-rate of the mass accretion history $d\log M/d\log a$, the scale radius R_s , and the density of the halo within 10 kpc. For each parameter the evolution of two halos with the same final mass (5×10^{12}) but different values of a_c (0.25 and 0.5) is shown. In the plot of the mass accretion rate, the value of S used to define a_c is marked with a thin dotted line.

results differ in detail from what we have found using N -body simulations, the general trends associated with early and late formation seem to agree. Our results may serve as a useful benchmark against which specific analytic and semi-analytic models of halo structure formation can be

tested.

The correlation we have found between individual halo assembly histories and their density profiles is likely to have important consequences for a large range of observable galaxy properties. For example, halo density profiles directly affect galaxy rotation curves, and are likely to play an important role in determining galaxy shapes, gas infall and star formation rates. We thus expect that the inclusion of such a correlation in the context of semi-analytic models which track galaxy formation and evolution with simple recipes will affect a number of predictions of these models, and thus will provide a significantly more realistic theoretical framework for understanding galaxy populations, the origin of galaxy type and the variation in galaxy properties.

ACKNOWLEDGMENTS

We thank Anatoly Klypin for useful discussions and for access to the simulations used for this analysis, which were performed at NRL and NCSA. We thank Tom Abel, George Blumenthal, Sandy Faber, Ari Maller, Piero Madau, Rachel Somerville, Frank van den Bosch, and David Weinberg for helpful discussions and comments. In addition, we thank the anonymous referee for several comments that improved the clarity of the manuscript. RHW received support from a GAANN fellowship at UCSC. JSB received support from NASA LTSA grant NAG5-3525 and NSF grant AST-9802568. AVK was supported by NASA through Hubble Fellowship grant from the Space Telescope Science Institute, which is operated by the Association of Universities for Research in Astronomy, Inc., under NASA contract NAS5-26555. This work was also supported by NASA ATP grant NAG5-8218, NSF grant PHY-0070940 and a Faculty Research Grant at UCSC, and by the US-Israel Bi-national Science Foundation grant 98-00217.

APPENDIX

FINDING AND FITTING HALOS

The details of our procedure for finding and fitting halos are as follows:

1. We construct density field values by a Cloud-in-Cell (CIC) process (Hockney & Eastwood 1981) on the largest grid of the simulation ΔL , and rank the particles according to their local density as determined on this grid. We then search for the possible halo centers, using two sets of smoothing spheres; one, with a small radius, r_{sp1} , in order to locate the centers of tight, small clumps; and the other, with a larger radius, r_{sp2} , in order to locate the centers of halos with diffuse cores. The larger radius, r_{sp2} , is set equal to $R_{\text{vir}}^{\text{min}}$, the virial radius of a halo of mass $M_{\text{vir}}^{\text{min}}$. The smaller radius is set to $r_{\text{sp1}} = 5R_{\text{vir}}^{\text{min}}/N_{\text{p}}^{\text{min}}$, a rough approximation to the radius within which our smallest halo would be expected to contain ~ 5 particles.

For each set of spheres, we take from the ranked list the particle with the highest local density and place a sphere about its location. A second sphere is placed about the next particle in the list not contained in the first sphere. The process is continued until all of particles are contained within at least one sphere. Because we are only interested in centers of halos more massive than $M_{\text{vir}}^{\text{min}}$, we discard each sphere with fewer than a set number of particles. The minimum number of particles required for a kept sphere is determined separately for each radius.

For the r_{sp1} spheres, we use the following conservative halo density profile:

$$\rho(r) = \begin{cases} C/r_{\text{sp1}}^{2.5} & r < r_{\text{sp1}} \\ C/r^{2.5} & r > r_{\text{sp1}}, \end{cases} \quad (\text{A1})$$

(where C is determined by fixing the minimum halo mass to be $M_{\text{vir}}^{\text{min}}$), in order to estimate the minimum number of particles within r_{sp1} :

$$N_{\text{sp1}} = \frac{N_{\text{p}}^{\text{min}}}{1 + 6[(R_{\text{vir}}^{\text{min}}/r_{\text{sp1}})^{1/2} - 1]}. \quad (\text{A2})$$

For the $z = 0$ output of the $60h^{-1}\text{Mpc}$ simulation we analyze, $N_{\text{sp1}} = 3$ (rounding to the next lowest integer). Spheres of size r_{sp1} with fewer than N_{sp1} particles are discarded. Similarly, all of the r_{sp2} spheres containing fewer than $N_{\text{sp2}} = N_{\text{p}}^{\text{min}}$ particles are discarded.

The final list of candidate halo centers is made up of all of the (small) r_{sp1} spheres, together with each of the r_{sp2} spheres that *does not* contain an r_{sp1} sphere.

2. For each sphere of radius $r_{\text{sp}} = r_{\text{sp1}}$ or r_{sp2} , whichever applies, we use the particle distribution within the sphere to find the center of mass and iterate until convergence. We repeat the procedure using a smaller radius, $r = r_i$, where $r_i = r_{\text{sp}}/2^{\frac{i}{2}}$. We continue this method until $r_i = r_L$, where r_L is defined by the criterion $r_L > 2f_{\text{res}} > r_{L+1}$, or until reduction leads to a sphere with fewer than N_{sp1} particles.
3. We unify the spheres whose centers are within r_L of each other. The unification is performed by making a density weighted guess for a common center of mass, and then iterating to find a center of mass for the unified object by counting particles. The size of sphere used to determine the center of mass is the smallest radius that will allow the new sphere to entirely contain both candidate halo spheres.
4. For each candidate halo center we step out in radial shells of $3f_{\text{res}}$, counting enclosed particles, in order to find the outer radius of the halo: $R_h = \min(R_{\text{vir}}, R_t)$. The radius R_{vir} is the virial radius, and R_t is a ‘‘truncation’’ radius, defined as the radius ($< R_{\text{vir}}$) in which a rise in (spherical) density is detected ($d \log \rho / d \log r > 0$). This is our method for estimating when a different halo starts to overlap with the current halo and is important for halos in crowded regions. We estimate the significance of a measured upturn using the Poisson noise associated with the number of particles in the radial bins considered. Only if the signal to noise of the upturn is larger than σ_{R_t} do we define a truncation radius. The value of σ_{R_t} is a free parameter. We use $\sigma_{R_t} = 5$.⁶
5. Among the halo candidates for which we have found an R_{vir} , we discard those with $N_{\text{vir}} < N_{\text{p}}^{\text{min}}$, where N_{vir} is the number of particles within R_{vir} . Among the halo candidates for which we have found a rise in spherical density, we discard those which contain less than $N_{R_t}^{\text{min}}$ particles, where $N_{R_t}^{\text{min}} = N_{\text{p}}^{\text{min}}$ if $R_t > R_{\text{vir}}^{\text{min}}$, otherwise

$$N_{R_t}^{\text{min}} = N_{\text{p}}^{\text{min}} \left(\frac{R_t}{R_{\text{vir}}^{\text{min}}} \right). \quad (\text{A3})$$

The above constraint follows from an extrapolation of the minimum mass halo using an isothermal profile $\rho(r) \propto 1/r^2$.

6. For halos with more than $N_{\text{p,fit}}^{\text{min}}$ particles, we model the density profile of each halo using the NFW form (Eq 1) and determine the best fit R_s and ρ_s values, which determine R_{vir} and M_{vir} . The fitting procedure uses logarithmically spaced radial bins from $\max(2f_{\text{res}}, 0.02 \times \min(R_{\text{vir}}, R_t))$ out to R_h . If any bins are empty we decrease the number of bins by one until this is no longer the case. If the number of bins is reduced below three we discard the halo as a local perturbation.

The fit takes into account the Poisson error in each bin due to the finite number of particles, and we obtain errors on the fit parameters (σ_{R_s} and σ_{ρ_s}) using the covariance matrix in the fit routine. The errors on the fit parameters can be translated easily into errors for R_{vir} ($\sigma_{R_{\text{vir}}}$) and the estimated NFW mass of each halo, M_{vir} (σ_M). In some cases, the fit does not converge. When this occurs, we mark the halo as a non-fit. This occurrence is rare for distinct halos, but is more common for subhalos (see below). This may reflect a tendency for subhalos defined with the current merging criteria to be poorly described by an NFW form, perhaps as a result of frequent interactions or close neighbors.

7. We unify halos with centers that overlap by R_{combine} . For a given pair of halos with virial radii $R_{\text{vir},1}$, $R_{\text{vir},2}$, we define this combination radius to be $R_{\text{combine}} = \min(R_{\text{vir},1}/2, R_{\text{vir},2}/2)$. If either of the halos does not have a fit R_{vir} , we use the halo radius R_h in place of R_{vir} . Our criterion is met if two (or more) halo centers are within R_{combine} of each other while at the same time having velocities which allow them to be bound to the common system. If such a case occurs, then along with the individual halo NFW fits, we fit another NFW profile about the common center of mass of the two combined halos and decide whether the candidate-united-halos are bound/unbound to the common NFW fit using the radial escape velocity determined using the common NFW profile (see below). If both halos are bound we combine the two halos into one, and keep the common fit for the characteristic parameters. If at least one is not bound, we do not combine the halos.
8. For each halo, we remove all unbound particles before we obtain the final fits. We loop over all particles within the halo and declare a particle at a distance r from the center of a halo to be unbound if its velocity relative to the center of mass velocity of the halo obeys $v > \sqrt{2|\Phi(r)|}$. For halos that have fits, we use the radial potential

⁶ The choice was motivated by several tests using mock catalogs of halos in clusters designed to determine how varying σ_{R_t} affects our ability to fit the density profiles of subhalos. Although our results were not strongly dependent on this choice, we did obtain the best fits using $\sigma_{R_t} = 5$.

for an NFW density profile⁷:

$$\Phi_{\text{NFW}}(r) = -4\pi G \rho_s R_s^2 \left[\frac{\log(1+x)}{x} \right]; \quad (\text{A4})$$

otherwise, we use the radial potential for a singular isothermal sphere with the same mass.

After removal, we construct a new density profile (and find new NFW fit parameters if $N_p \geq N_{p,\text{fit}}^{\text{min}}$). The procedure is repeated until the number of unbound particles becomes $< 1\%$ of the bound particles or until the total number of particles within the halo falls below N_p^{min} .

9. For each halo in the final catalog, we determine its NFW fit if $N_p \geq N_{p,\text{fit}}^{\text{min}}$, and record its fit parameters and their errors. We also measure and record its spin parameter, λ , and the maximum of its circular velocity curve, V_{max} .

As described above, the halo catalog we have developed includes an arbitrary number of levels of substructure within halos. The full catalog with substructure should then include all halos directly around galaxies, above the relevant mass resolution, and thus is useful for a number of direct comparisons with observations. However, for many purposes, a halo catalog including only “distinct” halos, i.e., halos which are not subhalos of any larger halo, is sufficient and introduces significantly less complication. For this reason we have culled the full catalog into a smaller catalog that does not include subhalos within halos; this is the catalog analyzed here.

Since there are multiple levels of substructure, the details depend slightly on the algorithm chosen. We take the maximum circular velocity to be the most reliable measure of the halo’s size, since it is a measured quantity and doesn’t rely on a fit, and can be defined equivalently for all halos. All halos whose centers lie within the virial radius of a larger halo are then designated as subhalos. Note that a halo that lies within the virial radius of subhalos is only removed if it itself is classified as a subhalo of a distinct halo.

CORRECTING MASSES

Our procedure of fitting density profiles is intended to give the best estimate possible of a halo’s virial mass; however, it is subject to large errors when there are a small number of particles or especially when the halo is undergoing merging or disruption and is far from being a relaxed, spherical object. These uncertainties are taken into account in the fit errors, but for many purposes it is essential to have the best estimate possible of the halo’s mass at each output time. Especially for consideration of the evolution of individual halo mass trajectories it would be useful to eliminate large jumps in the trajectories which are due to the above-mentioned irregularities and not to real changes in a halo’s mass. In order to do this, for each halo we compare three masses: M_{vir} , as measured from the NFW fit, M_h , the measured mass within R_h , and M_{traj} , which designates the mass interpolated between the most massive progenitor in the previous output time and the offspring halo in the subsequent output time (assuming they both exist). In most cases, $M = M_{\text{vir}}$ (if M_{vir} exists, otherwise $M = M_h$); it is only changed if this mass seems clearly inconsistent with the other mass estimates and does not seem reasonable. For most halos, the error on M_{vir} is small and $M_{\text{vir}} \simeq M_h$; in these cases M always equals M_{vir} . However, if one of these is not the case, M_{vir} is used if it is close to M_{traj} and otherwise M_h is used if it is close to M_{traj} . If neither seems consistent with the halo’s trajectory, we use $M = \text{median}(M_{\text{vir}}, M_h, M_{\text{traj}})$. The details of the procedure are slightly more complicated, depending on the error on M_{vir} , and we direct the reader to Wechsler (2001) for a complete description.

GENERATING MERGER TREES

For completeness, we outline here the fundamental aspects of EPS and our method for generating merger trees. Lacey & Cole (1993, hereafter LC93) introduced a method for calculating the probability that a halo of mass M accretes a given mass in a given time. Let $S(M) \equiv \sigma^2(M)$ be the linear density variance on the mass scale M and $w(t) \equiv \delta_c(t)$ be the linear density for collapsing structures at time t (see, e.g., White 1996). Given a halo of mass M at some time t , the probability that it accretes a mass ΔM in a time Δt is then

$$P(\Delta S, \Delta w) d\Delta S = \frac{1}{\sqrt{2\pi}} \frac{\Delta w}{(\Delta S)^{3/2}} \exp \left[-\frac{(\Delta w)^2}{2\Delta S} \right] d\Delta S, \quad (\text{C1})$$

where $\Delta S = S(M) - S(M + \Delta M)$ and $\Delta w = w(t) - w(t_1 + \Delta t)$. In order to generate halo merging trees, one must implement this formula iteratively, with some algorithm for choosing progenitors. However, no method has been proposed that simultaneously matches the the conditional mass function and progenitor distribution of specified by Eq. C1 exactly. We use the scheme suggested by Somerville & Kolatt (1999, SK99), which enforces mass conservation exactly but only reproduces the progenitor distribution of EPS approximately (for alternative techniques see Kauffmann et al. 1993 and LC93). In order to keep the trees finite, a minimum progenitor mass, M_m is defined. Halo mass growth with $\Delta M < M_m$ is treated as diffuse accretion. A key ingredient of this technique is that the timestep must be chosen such that $\Delta w \lesssim \sqrt{M_m dS/dM}$ in order to reproduce the expected conditional mass functions of extended Press-Schechter. Stepping back in time, the tree then provides a list of progenitors and their masses. In order to better match the analytic prediction

⁷ Note that this potential is *not* necessarily the physical gravitational potential at the halo location. For a subhalo, for example, the host background potential is *not* included.

of the progenitor distribution, we apply an addition fix to the method of SK99, suggested by Bullock et al. (2000), which constrains the number of progenitors at any timestep to be close to the mean for that mass and redshift.

n

REFERENCES

- Avila-Reese, V., Colín, P., Valenzuela, O., D’Onghia, E., & Firmani, C. 2001, *ApJ*, 559, 516
- Avila-Reese, V., Firmani, C., & Hernández, X. 1998, *ApJ*, 505, 37
- Avila-Reese, V., Firmani, C., Klypin, A., & Kravtsov, A. V. 1999, *MNRAS*, 310, 527
- Blumenthal, G. R., Faber, S. M., Primack, J. R., & Rees, M. J. 1984, *Nature*, 311, 517
- Bode, P., Ostriker, J. P., & Turok, N. 2001, *ApJ*, 556, 93
- Bond, J. R., Cole, S., Efstathiou, G., & Kaiser, N. 1991, *ApJ*, 379, 440
- Bryan, G. L. & Norman, M. L. 1998, *ApJ*, 495, 80
- Bullock, J. S. 1999, PhD thesis, University of California, Santa Cruz
- Bullock, J. S., Kolatt, T. S., Sigad, Y., Somerville, R. S., Kravtsov, A. V., Klypin, A. A., Primack, J. R., & Dekel, A. 2001, *MNRAS*, 321, 559, (B01)
- Bullock, J. S., Kravtsov, A. V., & Weinberg, D. 2000, *ApJ*, 539, 517
- Cohn, J. D., Bagla, J. S., & White, M. 2001, *MNRAS*, 325, 1053
- Craig, M. W. 1997, PhD thesis, University of California, Berkeley
- Davis, M., Efstathiou, G., Frenk, C. S., & White, S. D. M. 1985, *ApJ*, 292, 371
- Dubinski, J. & Carlberg, R. G. 1991, *ApJ*, 378, 496
- Efstathiou, G., Frenk, C. S., White, S. D. M., & Davis, M. 1988, *MNRAS*, 235, 715
- Eke, V., Navarro, J., & Steinmetz, M. 2001, *ApJ*, 554, 114
- Frenk, C. S., White, S. D. M., Davis, M., & Efstathiou, G. 1988, *ApJ*, 327, 507
- Gardner, J. 2001, *ApJ*, 557, 616
- Ghigna, S., Moore, B., Governato, F., Lake, G., Quinn, T., & Stadel, J. 2000, *ApJ*, 544, 616
- Gross, M. A. K., Somerville, R. S., Primack, J. R., Holtzman, J., & Klypin, A. 1998, *MNRAS*, 301, 81
- Hockney, R. W. & Eastwood, J. W. 1981, *Computer Simulation Using Particles* (Computer Simulation Using Particles, New York: McGraw-Hill, 1981)
- Jenkins, A., Frenk, C. S., White, S. D. M., Colberg, J. M., Cole, S., Evrard, A. E., Couchman, H. M. P., & Yoshida, N. 2001, *MNRAS*, 321, 372
- Jing, Y. P. 2000, *ApJ*, 535, 30
- Kauffmann, G., White, S. D. M., & Guiderdoni, B. 1993, *MNRAS*, 264, 201
- Klypin, A. A. & Holtzman, J. 1997, astro-ph/9712217
- Klypin, A. A., Kravtsov, A. V., Bullock, J. S., & Primack, J. R. 2001, *ApJ*, 554, 903
- Kravtsov, A. V., Klypin, A. A., & Khokhlov, A. M. 1997, *ApJS*, 111, 73
- Lacey, C. & Cole, S. 1993, *MNRAS*, 262, 627
- Moore, B., Governato, F., Quinn, T., Stadel, J., & Lake, G. 1998, *ApJ*, 499, L5
- Navarro, J. F., Frenk, C. S., & White, S. D. M. 1995, *MNRAS*, 275, 56
- . 1996, *ApJ*, 462, 563
- . 1997, *ApJ*, 490, 493
- Peebles, P. J. E. 1982, *ApJ*, 263, L1
- Press, W. H. & Schechter, P. 1974, *ApJ*, 187, 425
- Ryden, B. S. & Gunn, J. E. 1987, *ApJ*, 318, 15
- Sheth, R. K., Mo, H. J., & Tormen, G. 2001, *MNRAS*, 323, 1
- Sheth, R. K. & Tormen, G. 1999, *MNRAS*, 308, 119
- . 2001, preprint, astro-ph/0105113
- Somerville, R. S. & Kolatt, T. S. 1999, *MNRAS*, 305, 1
- Somerville, R. S., Lemson, G., Kolatt, T. S., & Dekel, A. 2000, *MNRAS*, 316, 479, (SLKD)
- Taylor, J. E. & Navarro, J. F. 2001, *ApJ*, in press, astro-ph/0104002
- van den Bosch, F. C. 2000, *ApJ*, 530, 177
- . 2001, preprint, astro-ph/0105158
- Vitvitska, M., Klypin, A. A., Kravtsov, A. V., Bullock, J., Wechsler, R. H., & Primack, J. R. 2001, preprint, astro-ph/0105349
- Wechsler, R. H. 2001, PhD thesis, University of California, Santa Cruz
- White, S. D. M. 1996, in *Cosmology and Large-Scale Structure*, ed. R. Schaeffer, J. Silk, & J. Zinn-Justin (Dordrecht: Elsevier Science)
- Zaroubi, S. & Hoffman, Y. 1993, *ApJ*, 416, 410